5

Mass Inertia Effect based Vibration Control Systems for Civil Engineering Structure and Infrastructure

Chunwei Zhang and Jinping Ou
Harbin Institute of Technology, Harbin, Dalian University of Technology, Dalian, P.R.China

1. Introduction

In 1972, J.T.P. Yao introduced the modern control theory into vibration control of civil structures (Yao, 1972), which started the new era of research on structural active control in civil engineering field. During the development of nearly 40 years, Active Mass Driver/Damper (AMD) control, with the better control effect and cheaper control cost, has taken the lead in various active control occasions, becoming the most extensively used and researched control systems in lots of practical applications (Soong, 1990; Housner *etal.*, 1997; Spencer *etal.*, 1997; Ou, 2003). Several important journals in civil engineering field, such as ASCE Journal of Engineering Mechanics (issue *4th*, in 2004), ASCE Journal of Structural Engineering (issue *7th*, in 2003), Earthquake Engineering and Structural Dynamics (issue *11th*, in 2001 and issue *11th*, in 1998), reviewed the-state-of-the-art in research and engineering applications of semi-active control and active control, especially AMD control. In addition, Spencer and Nagarajaiah (2003) systematically overviewed the applications of active control in civil engineering. Up to date, more than 50 high-rising buildings, television towers and about 15 large-scale bridge towers have been equipped with AMD control systems for reducing wind-induced vibration or earthquake-induced vibration of the structures.

Besides, there are quite a number of successful applications with passive Tuned Mass Damper (TMD) control system, from wind induced vibration control of long-span bridge towers and building structures, to chimneys and mast structures; from the first applications of the collapsed World Trade Center towers and coetaneous John Hancock building etc., which were built in 1960s, to recently built highest structures in the world, *e.g.* Twin towers in Kulua- Lumpur in Malaysia, 101 skyscraper in Taipei city and Guangzhou New TV tower in China etc. It can be seen from these applications, the implementation of incorporating Mass Driver/Damper based vibration control systems for protection of Civil Engineering structures and infrastructures against wind and earthquake excitations, have already been widely accepted by the field researchers as well as engineer societies.

2. EMD control systems

Zhang (2005) made a systematically comparison for different control schemes under the background of the Benchmark control problem, and disclosed that the AMD control was the

Source: Vibration Control, Book edited by: Dr. Mickaël Lallart,
ISBN 978-953-307-117-6, pp. 380, September 2010, Sciyo, Croatia, downloaded from SCIYO.COM

best control scheme due to these merits, such as the best ratio of control effect over control effort, simple and easy to be implemented etc. Moreover, through analysis of typical important large-scale structures subjected to different excitations, the effectiveness and feasibility of employing AMD control for civil structures has been successfully proven (Ou, 2003; Zhang, 2005), where wind and earthquake induced vibration control of high-rising buildings and bridge towers, ice induced vibration control of offshore platforms, wind-wave-current coupling excited control of deep sea platforms are all studied. Usually, an AMD control system is composed of a mass piece, an actuator, stiffness component (coil spring is commonly used), a damper, a stroke limiting device, a brake protector, sensors, a data acquisition and processing system, computerized real-time control software and hardware system (Dyke *etal.*, 1994, 1996; Quast *etal.*, 1995; Spencer *etal.*, 1997). In addition, a power supplying system is needed for operating all the electrical devices mentioned above.
In traditional AMD system, the mostly used actuators are hydraulic cylinders or electrical servo motors, which may have the following disadvantages, such as large in system volume, complicated in construction, time delay, slow to response, and limited mass stroke etc. Aiming at this, several new special devices were put forward to replace the traditional actuators (Haertling, 1994, 1997; Nerves, 1996; Scruggs, 2003). Learning from the motion control principle of magnetic suspended vehicle, the electromagnetic mass damper (subsequently called the "EMD") control system, as an innovative active control system, was proposed for structural vibration control (Zhang, 2005), which uses the driving technology of linear electric machines, transforming the electric energy directly into mechanical energy of EMD system, for example, the kinetic energy of EMD mass. Figure 1(a) shows the conception sketch of hydraulic actuated AMD system and its implementation illustration in a typical structural model, as shown in figure 1(b). By comparison, figure 2(a) and 2(b) shows the corresponding sketch and implementation sketch of the EMD control system.

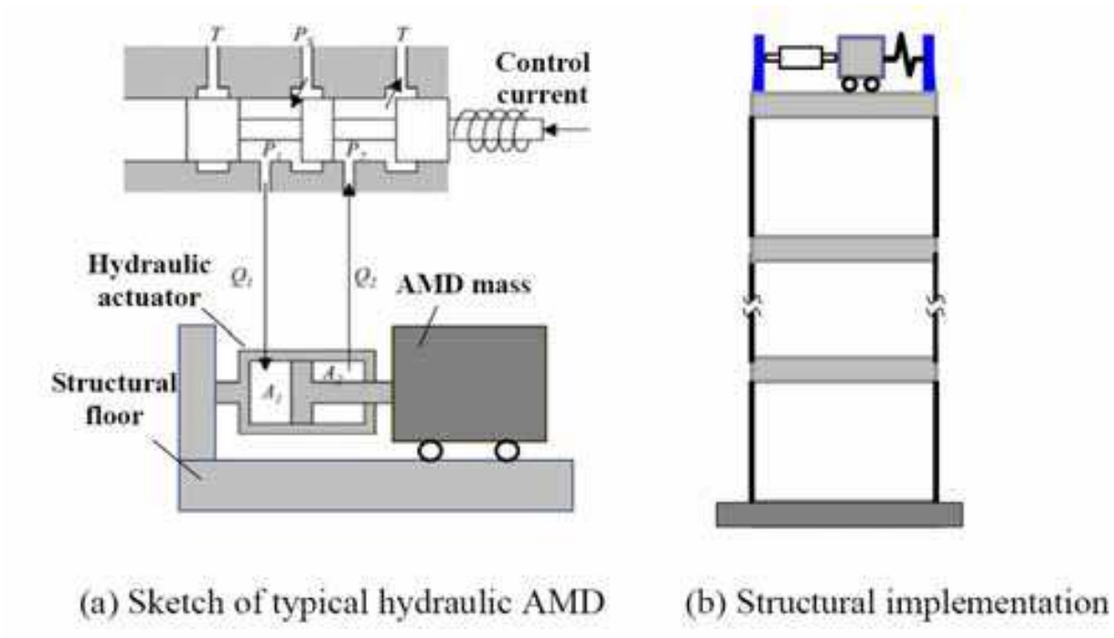

Fig. 1. Sketch of structure with hydraylic actuated AMD control System

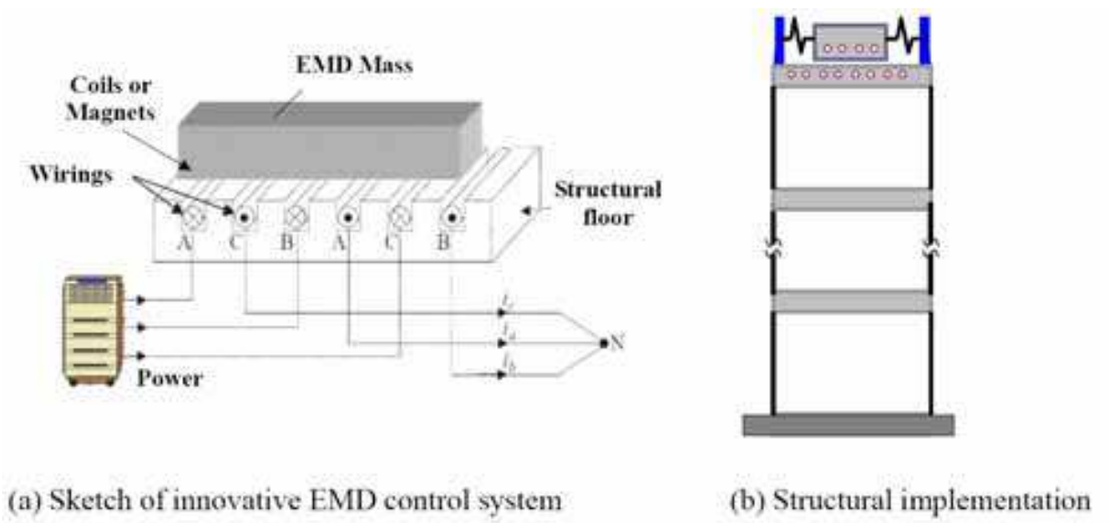

Fig. 2. Sketch of structure with Electromagnetic Mass Damper (EMD) contol system

2.1 Miniature EMD control system

The miniature experimental EMD control system is composed of a mass piece (direct current excitation coils encapsulated in high-strength engineering plastics, with mounting holes on its surface), a permanent magnet rod made of high energy rare earth material, linear sliding bearings and the system chassis. In addition, in order to form a closed-loop EMD system, an optical scale and an accelerometer are integrated into the EMD system to measure the stroke and absolute acceleration of the mass, respectively. Photo of the whole integrated system is shown in figure 3.

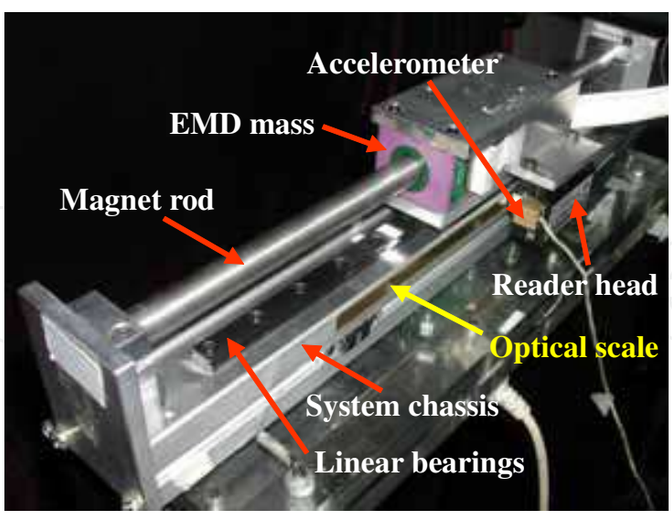

Fig. 3. Integrated photo of the EMD actuator

The excitation coil in the sealed mass package is 87mm long, made by Copley Controls Inc., and the whole mass piece weighs 186 grams. The permanent magnet rod is 332mm long with the diameter of 11mm. The main electrical specifications of this EMD system are: peak force constant is 5.74N/A, root mean square (RMS) force constant is 8.12N/A, back electro-

motive force (EMF) constant is 6.63 $V \cdot s/m$, the coil resistance at 25°C is 5.35 Ω , and the coil inductance is 1.73mH. The mass stroke of EMD system is measured using a Renishaw optical scale, which is pasted onto the system chassis as shown in the photo above, while the reading head is fixed on the side wall of EMD mass. The reading head model is RGH24 with the resolution of 2-micro-meter, and the scale is 220mm long. In addition, one tiny accelerometer (type DH201-050) is installed on the prolonging side-wall of the EMD mass with the measuring range of ±50g. This accelerometer is very compact indeed, with a weight of only two grams and a volume of 10mm×10mm×5mm, and it can be conveniently attached to any part of the mass piece without influencing the operation of the whole system.

2.1.1 System mathematical models

From the aspect of circuit calculation, the armature of EMD system consists of three parts: motor coil which is capable of outputting mechanical force or energy, coil inductance and coil resistance. According to the Kirchhoff's first principle, the relationship of the circuit voltage and current can be written as

$$L_m \frac{di(t)}{dt} + R_m i(t) + \varepsilon(t) = V_m(t) \tag{1}$$

Where L_m is the coil inductance, R_m is the coil resistance, $V_m(t)$ is the input voltage, $\varepsilon(t)$ is the inducted back EMF constant, $i(t)$ is the current intensity in the coil.

Defining the following two electric indices of linear motors, $K_f = \frac{F_{\text{EMD}}}{I}$ standing for force constant which means electromagnetic force generated by unit current input, and $K_m = \frac{\varepsilon}{v}$ standing for the back EMF constant which means back EMF generated by unit velocity, then the following relationships are reached,

$$i(t) = F_{\text{EMD}} / K_f \; ; \; \varepsilon(t) = K_m v \tag{2}$$

Substituting equation (2) into equation (1) gives

$$L_m \frac{dF(t)}{dt} \frac{1}{K_f} + \frac{R_m}{K_f} F(t) + K_m v(t) = V_m(t) \tag{3}$$

After proper transformation, equation (3) can be rewritten as,

$$F(t) = \frac{K_f}{R_m} V_m(t) - \frac{K_f K_m}{R_m} \dot{x}_a(t) - \frac{L_m}{R_m} \frac{dF(t)}{dt} \tag{4}$$

Where $\dot{x}_a$ is the relative velocity of EMD mass, and F(t) is the controllable electromagnetic force.

2.1.2 System dynamic tests

During dynamical tests, the EMD system is fixed on the shaking table, and the system coil is powered with the ASP-055-18 servo amplifier, with a DC current output of 0~10A and voltage of 0~55V. The power supply is the HB17600SL series regulator module. A series of

sine position based tests under Position-velocity control of large mass strokes and low frequencies are conducted.

For example, figure 4 shows the hysteresis loops of control force versus velocity and circuit current, respectively. From the force-current relationship, fine linear relationship again indicates the EMD system to be a linear actuator under low operating frequencies, with high ability in dissipating energy at the same time.

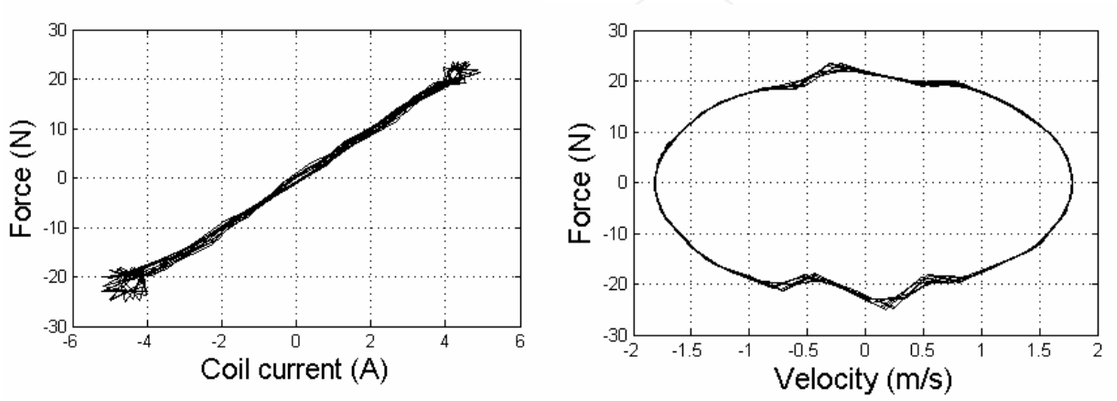

Fig. 4. Force hysteresis loops of EMD system

2.1.3 Experimental implementation of structural model

The test structural model employed in this part is a two-story shearing type structure, called the Bench-scale structure, manufactured by Quanser Inc., which has been designed to study critical aspects of structural control implementations and widely used in education or research of civil engineering and earthquake engineering throughout the world (Battaini, 2000; Quanser, 2002). The column of the test structure is made of thin steel plate, 2mm thick, and the floors are made of plastic, 13mm thick, and the inter-storey height of the structure is 490mm. Shaker-II table, made by Quanser Inc., is employed here for generating earthquake excitations as well as other excitations to be exerted onto the test structure. Through sine sweep test, the natural frequencies of the structure are found to be 1.27Hz and 4.625Hz corresponding to the first two dominant vibration modes respectively, where the mass of the EMD system is fixed on the top floor, named as uncontrolled case. The photo of the whole experimental system and its calculation sketch are shown in figure 5.

In the current experimental setup, two accelerometers are installed under each floor and another accelerometer ia installed on the shaking table surface to measure structural response and input excitation respectively. The acceleration transducers are the type of Kistler K-Beam 8034A with the measuring range being ±2.0g and the sensitivity gain being 1024mV/g. Two laser displacement sensors, type of Keyence LK-2501/2503, are employed to measure the absolute displacement of each floor of the structure, which both work under the long distance mode, and the measuring range is ±250mm with the gain being 200mV/cm. Here the displacement measurement is used only for verification purpose, while not for feedback.

In this section, shaking table tests of structural seismic response control employing the EMD system were conducted, where three benchmark earthquake waves were used as input to examine the control effectiveness of such an innovative active control system, and typical results under Kobe earthquake wave (NS, January 17, 1995) input will be shown in the

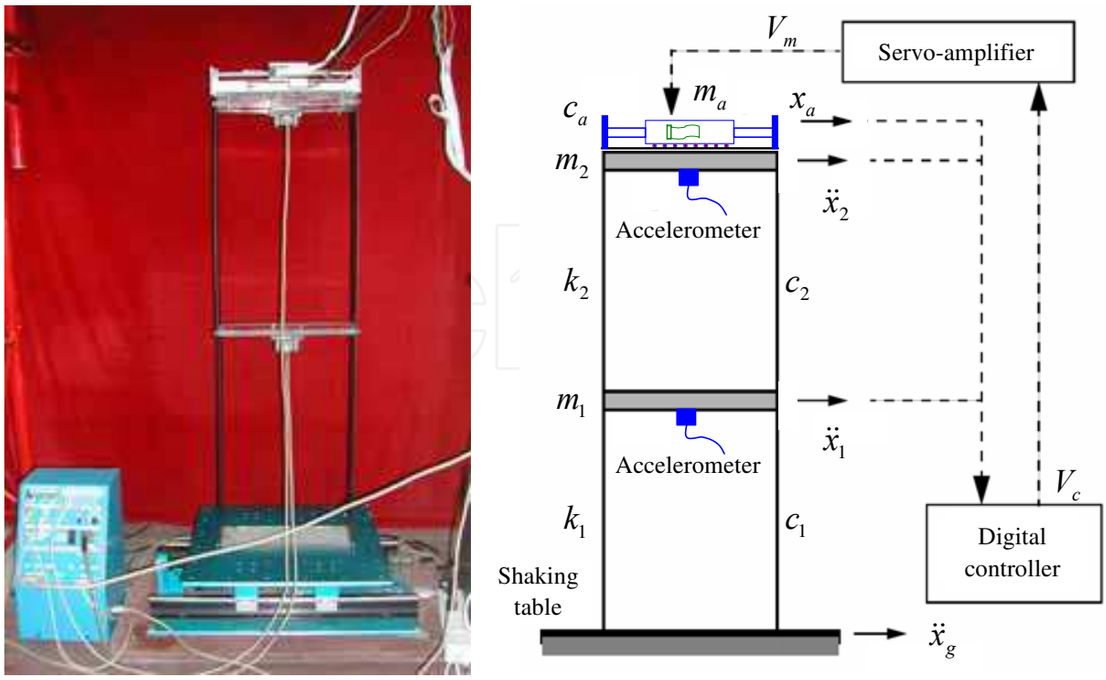

Fig. 5. Photo and calculation sketch of whole system

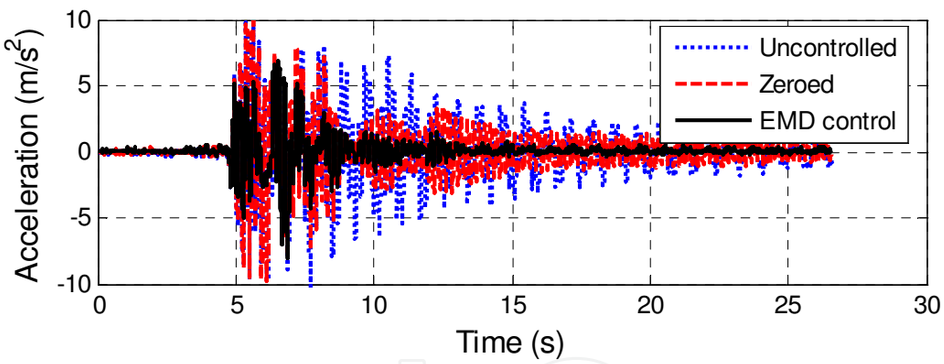

(a) Absolute acceleration of the first floor

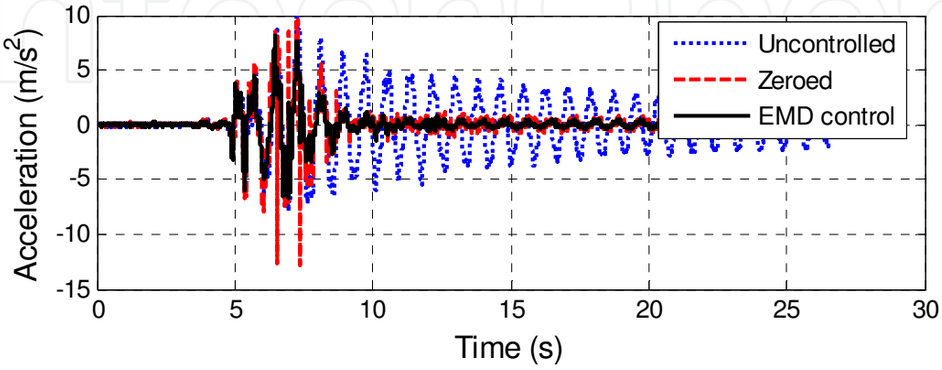

(b) Absolute acceleration of the top floor

Fig. 6. Experimental structural acceleration under Kobe wave excitation

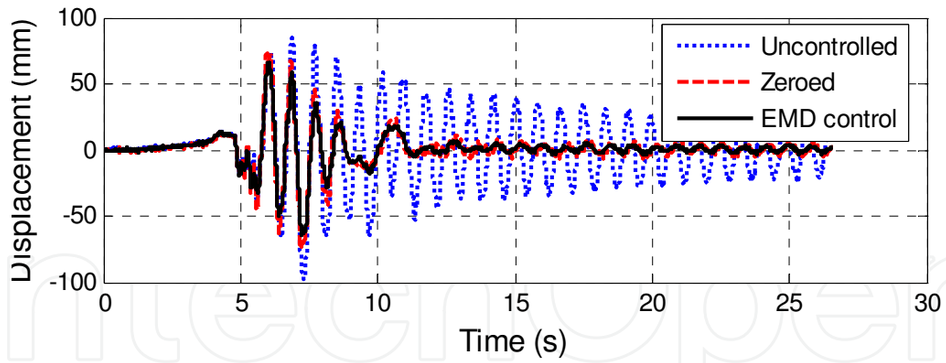

(a) Absolute displacement of the first floor

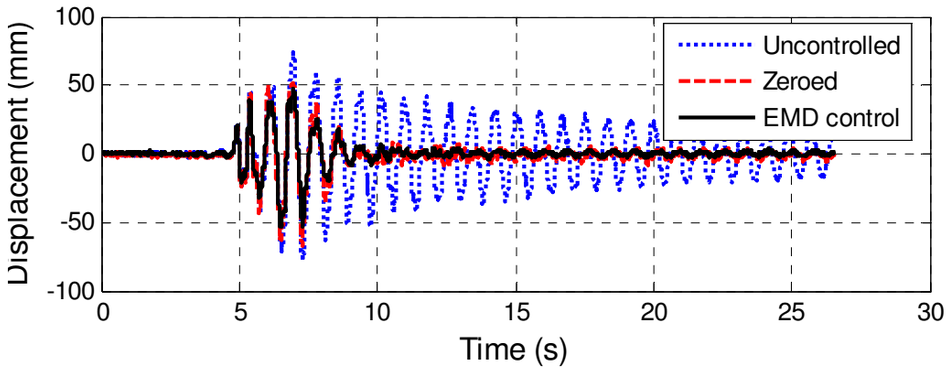

(b) Inter-drift of the top floor

Fig. 7. Experimental structural displacement under Kobe wave excitation

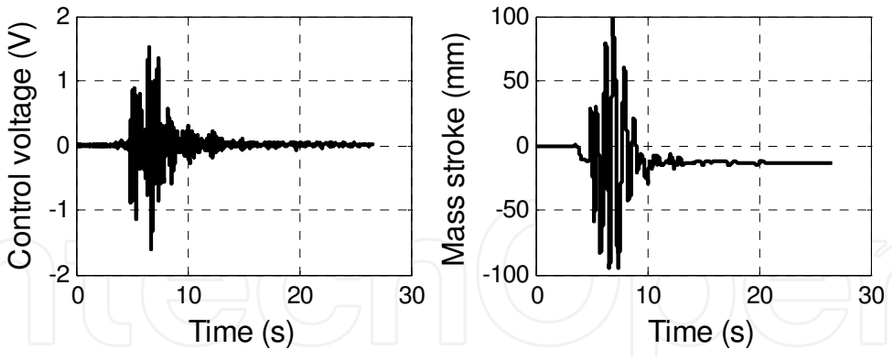

Fig. 8. Time history of control voltage and mass stroke of EMD system under Kobe wave excitation

following part. During the experiment, laser transducers are used to measure the absolute displacements of each floor of the test structure, and the inter-storey deformation can be calculated through subtraction of displacements of adjacent floors.

Figure 6 and figure 7 show the comparison of the structural absolute acceleration and floor displacement and inter-drift under three cases, Uncontrolled, Zeroed and EMD active control respectively. From the results, the EMD control is shown to be the most effective in suppressing structural vibrations. In addition, time histories of control voltage and mass stroke of the EMD system are also shown in figure 8.

In the above, theoretical modeling, dynamical testing, shaking table tests have been systematically carried out for the miniature EMD control to investigate its feasibility for using in structural vibration control. All the results show it to be a promising active control system for civil engineering.

2.2 Benchmark scale EMD control system

The existing linear motor products are already getting so close to rotatory motors in velocitty regulation area, and the products are mostly low power motors to drive the AMD mass (Zong etal.,2002). Requested performances of AMD system used for vibration control of civil engineering structures are high power, heavy load and high response ability to frequency, however control accuracy is not necessarily requested. Sometimes the servo motor power may exceed hundreds or thousands of Kilowatts. One of the possible means to solve the problems is to use simple tri-phase asynchronous linear motors in the design of full scale AMD control system.

An approach of setting up the high power linear electrical motor servo system is studied in this part. To build the high power position servo system, normal frequency transducer is used to drive an asynchronous linear motor. Because the mathematical model of asynchronous motor is not easy to set up, a new controller design method based on the step response of the closed-loop system is introduced, and series of numerical simulations and experimental verifications were carried out. Experimental results showed that good control performance can be achieved using the designed controller for the physical system.

2.2.1 Principles of position control for asynchronous linear motor

Constitution of traditional rotatory position servo systems is shown in figure 9. In the traditional structure, rotatory machines and ball bearing screw are used, and the mass load is driven to perform linear motion. Due to the avoidless clearance between screw and load, transmission accuracy gets declined and the servo rigidity is affected. Linear motors are taken in to drive the load in the linear electric motor position servo system shown in figure 10. Without transmission components and movement transform, higher transmission accuracy and servo rigidity are achieved from asynchronous motors. At the same time, higher accuracy and dependability are achieved from whole position closed-loop system with raster ruler instead of rotatory encoder than half closed-loop system.

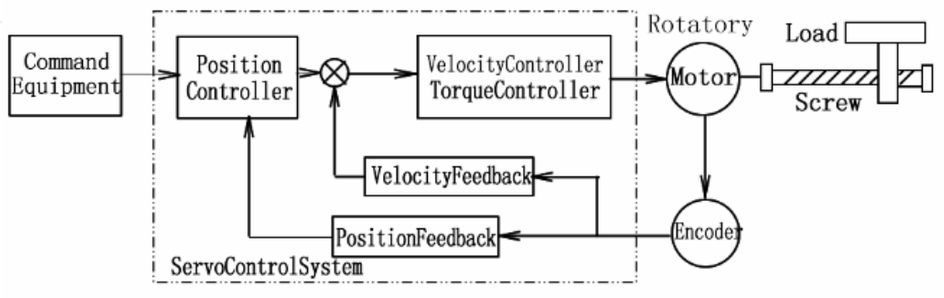

Fig. 9. Sketch of Rotary Servo System for Position Control

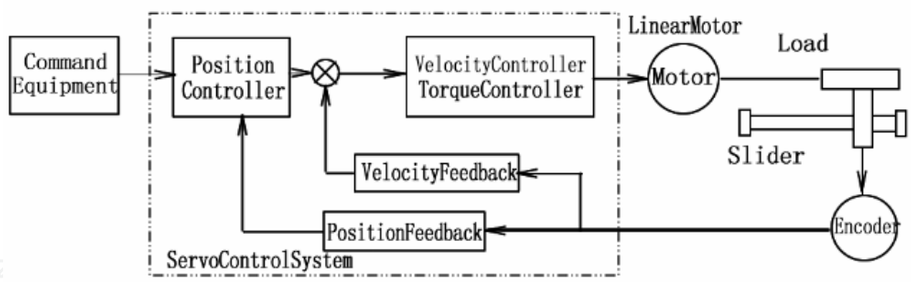

Fig. 10. Sketch of Linear Servo System for Position Control

Applications of linear motors focus on low power situations such as disk reader, printer, and numerical machine tools, so high power linear motion servo driver equipments can't be purchased. All the correlative hardware equipments have to be designed independently (Ye, 2003). This part takes vector alternating frequency transducer driver and asynchronous linear motor instead of position servo system, and makes use of computer servo control card to perform the controller's function, then builds the integrated servo system with asynchronous linear motor. The frame of the whole system is shown in figure 11.

From figure 11, functions of the components are shown: Control computer plays the role of servo controller. The position command signal is generated in MatLab/Simulink. Position error is calculated out from position command and position feedback from raster ruler, then velocity command signal is calculated, at last velocity voltage is produced from real-time control software WinCon and servo control card to frequency transducer. The linear motor is driven by the frequency transducer to run at the assigned speed according to the velocity command. The load is driven by the linear motor to perform linear motion displacement following the position command.

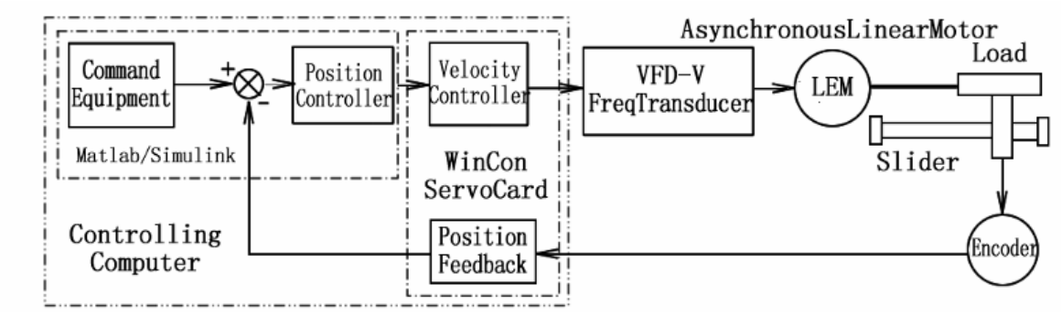

Fig. 11. Position Control of Asynchronous Linear Motor

Based on the structure shown in figure 11, equipments are chosen according to the power requirement. A tri-phase asynchronous linear motor with the power 4.5 kW, synchronous speed 4.5 m/s (50 Hz) is ordered, and a speed slip of 0.05 (5%) is estimated from experiments. The linear motor driver is Delta VFD-V model, high performance vector tri-phase alternating frequency transducer, with driving power of 5.5 kW. Position feedback tache is the most important component of the whole system, so a raster ruler produced by Renishaw Co. is chosen. Model of the ruler reader is RGS20, and minimal resolving power of the raster is 20 um. MultiQ-3 servo control card produced by Quanser Co. is setup in the control computer, with software of WinCon3.2 and Matlab 6.0. Structure of the whole

asynchronous linear electric motor is shown in figure 12. Figure 13 shows the picture of the experiment equipment and the software runtime is shown in figure 14.

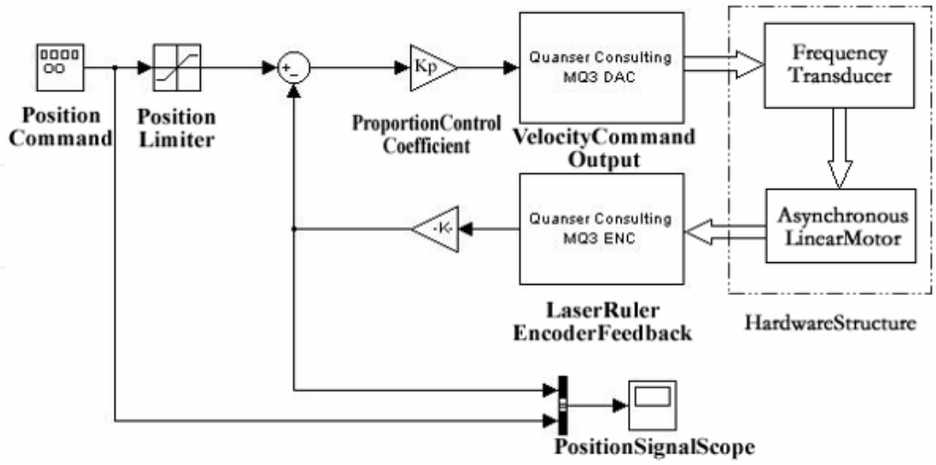

Fig. 12. Structure of the Position Control System

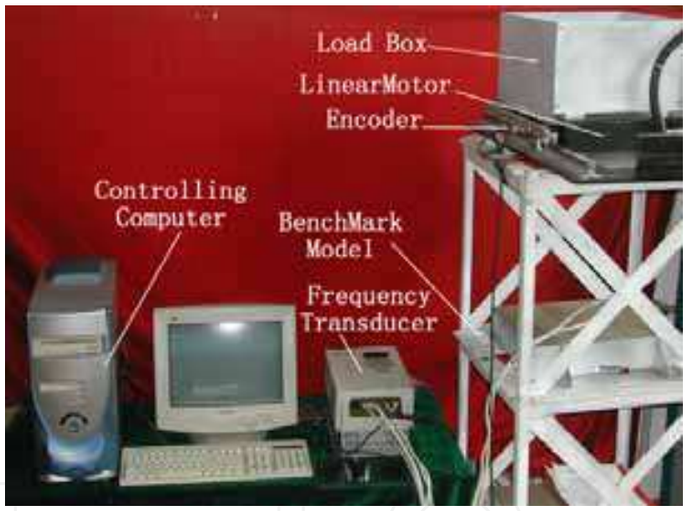

Fig. 13. Picture of the Control System

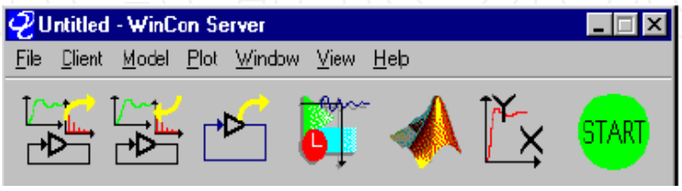

Fig. 14. Picture of the running WinCon

2.2.2 System model and position controller design

Traditional control method and controller design is commonly based on mathematics model of the object under control, and the controller is calculated according to required performance. Generally, mathematics model of the system is obtained by the method of analyze or system

identify, estimating model from the input and output experimental data. For the mathematic expression of asynchronous linear motor is so complex and parameters the manufacturer offered is not enough to build the model from analyze. At the same time, experiment situation of linear motor is limited by dimensions of the platform, so experiments can't be implemented to get enough data system identify required, which makes design of the controller much more difficult. In the engineering problem design process, simplification of the mathematics model usually makes the controller difficult to actualize or get awful performance. So a simple and facile approach that fits the engineering application is necessary.

This part analyzes and summarizes most of the design methods and tries a new design method. Reference to the design method of Extraction of Features of Object's Response, briefly EFOR, an approach to design the Lag-Lead compensator based on the experimental step response of the closed-loop system is implemented and good performances is achieved. Basic idea of quondam EFOR method is described as below: closed-loop simulation is carried out to a series of "Normal Object", to get the step response, and then some main time characteristic parameters are read out, and the controller is designed according to the parameters. The "Normal Object" is provided with some special characters: transfer function is strict proper rational point expression or proper rational point expression; minimum phase; at most one layer integral calculus; magnitude-frequency character is monotonous reduced function to the frequency (Wu etal., 2003).

Experiments showed that the asynchronous linear motor system couldn't satisfy all the requirement of the "Normal Object", especially the magnitude-frequency character is not monotonous reduced function to the frequency. But the step response of closed-loop system is similar to the attenuation oscillatory of the second-order system, so the EFOR method could be attempted to design the controller. So reference to the EFOR design method, a new method of Lag-Lead compensator design based on the experimental test is tried to accomplish the controller design. Detailed design process is shown below:

a. Step response experiment is carried out, especially the curve of high oscillatory with similar amplitudes, and attenuation oscillatory periods T_d is obtained, and then the frequency of system attenuation oscillatory $\omega_d = 2\pi / T_d$ is calculated, at last the critical attenuation oscillatory ω_p is estimated; The experimental method is especially fit for some systems which only perform movement within limited displacement such as linear electric motors. These systems have only limit experiment situation and can't perform long time experiments. The curve of high oscillatory with similar amplitudes when the proportion control coefficient is *Kp*=15 from the experiments is shown in figure 15.
   Parameters below are obtained:

$$T_d = 2.926 - 1.702 = 1.224s \tag{5}$$

$$\omega_p \approx \omega_d = 2\pi / T_d = 5.133 rad / s \tag{6}$$

   The Lag-Lead compensator is designed according to equivalence oscillatory frequency. Structure of the lead compensator is shown below:

$$K_h(s) = \frac{\frac{s}{\omega_m / \lambda} + 1}{\frac{s}{\lambda \omega_m} + 1} = \lambda^2 \frac{s + \frac{\omega_m}{\lambda}}{s + \lambda \omega_m} \qquad (\lambda > 1) \tag{7}$$

   Design of the lead compensator is mainly the chosen of parameters λ and ω_m .

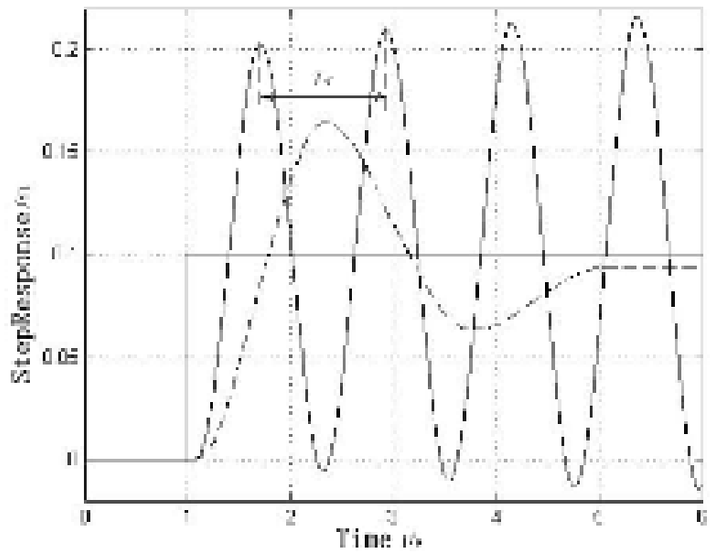

Fig. 15. Curve of Critical Oscillating System from Experiments

Parameter λ is named compensator strength. Larger λ produces plus phase excursion and better performance; too larger λ produces phase excursion increased not evidently, but makes the higher frequency gain so large that the high frequency noise is enlarged. So the λ should be selected based on the exceed quantity λ, usually from the empirical formula

$$\lambda = \begin{cases} 1.2 + 4\sigma & (\sigma \le 0.6) \\ 3.6 & (\sigma > 0.6) \end{cases} \tag{8}$$

So the compensator strength for the current system is $\lambda = 3.6$.

The compensator mid-frequency ω_m should be a little higher than ω_p . For the second-order system, usually from the empirical formula $\omega_m = \sqrt{\lambda}\omega_p$, so

$$\begin{aligned} \omega_m &= \sqrt{\lambda}\omega_p = \sqrt{3.6} \times 5.133 \\ &= 9.740 rad / s \end{aligned} \tag{9}$$

Thereby the lead compensator is achieved:

$$K_h(s) = \frac{\frac{s}{\omega_m / \lambda} + 1}{\frac{s}{\lambda\omega_m} + 1} = \frac{0.37s + 1}{0.0285s + 1} \tag{10}$$

b. The main purpose of the lag compensator is to reduce the stable error, but phase will usually be reduced, too, so the lag compensator parameters should be determined by the steady error after the lead compensator added. For the system that the error fits the requirement, a lag compensator is not necessary. Usually structure of the lag compensator is like this:

$$K_1(s) = \frac{s + \omega_1}{s + \rho\omega_1} \tag{11}$$

In the expression, the compensator strength is $0 < \rho < 1$. ω_1 is the seamed frequency of the lag compensator, so it must be lower than magnitude crossing frequency ω_c and not close to ω_c, to reduce the effect to mid-frequency performance. Usually $\omega_1 \approx (0.1 \sim 0.2)\omega_c$, $\rho = 1/n$, so that the steady error could be reduced to *1/n*。

Accordingly, the position controller is designed for the system. The perfect proportion control coefficient is *Kp*=8. Figure 16 shows the controller structure.

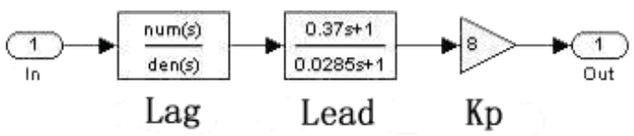

Fig. 16. Structure of Lag-Lead Controller

2.2.3 Simulation and experimental results

The lag-lead compensator based on the step response is $K_h(s) = (0.37s + 1)/(0.0285s + 1)$, and the perfect proportion control coefficient is *Kp*=8. With the method of getting controller coefficient from test-run, the best perfect coefficient for only proportion controller is *Kp*=8, and the best perfect coefficient for proportion differential controller is *Kp*=8, *Kd*=0.4. The coefficients are applied in the simulations and the experiments below.

By analyzing parameters of the lag-lead compensator and some conclusion from system identification, a simplification model was estimated to test the performance of the controllers. Simulations using different controllers such as lag-lead compensator, proportion controller, or proportion differential controller were carried out with the help of Matlab software. Simulation result with different controllers is shown in figure 17.

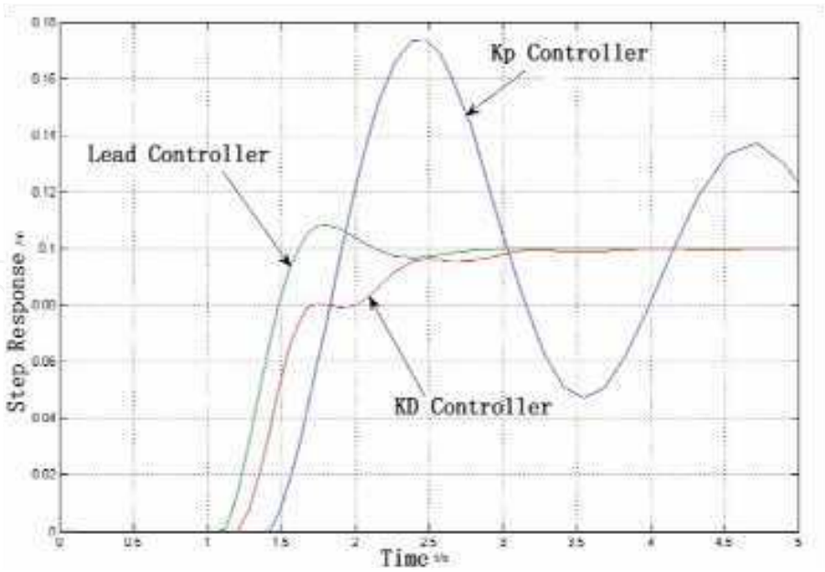

Fig. 17. Results of the Simulations using three different controllers

The figure shows that the lead compensator and the proportion differential controller make great improvement to the object under control. Compared with simple proportion controller, the response speed and the position control error are reduced a lot.

Some experiments were performed on the mechanic equipments. Figure 18 shows the performance of the lead compensator while adjusting the proportion coefficient near *Kp*=8. The performance of following ability test under the lead compensator is shown in figure 19. Obvious following effect to the sine position command with magnitude 50mm and frequency 1Hz is obtained.

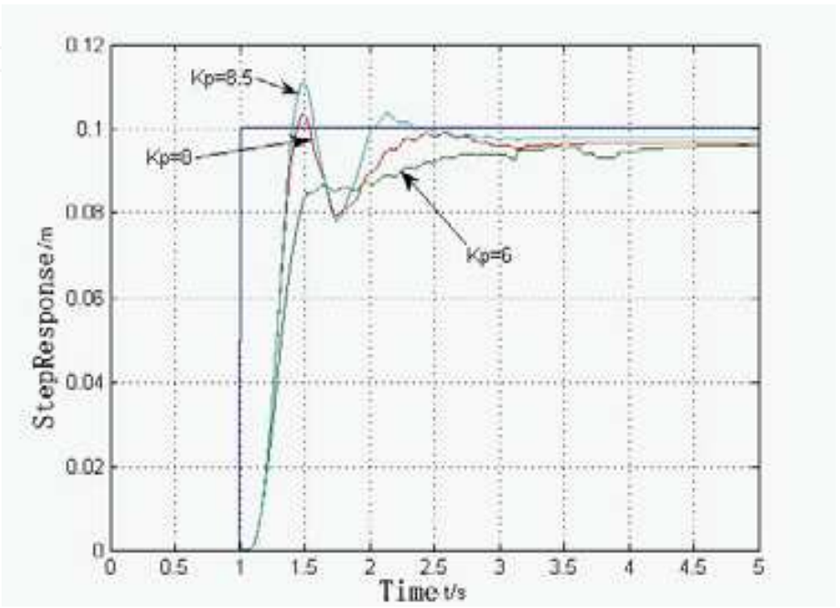

Fig. 18. Experiment Results using different Kp

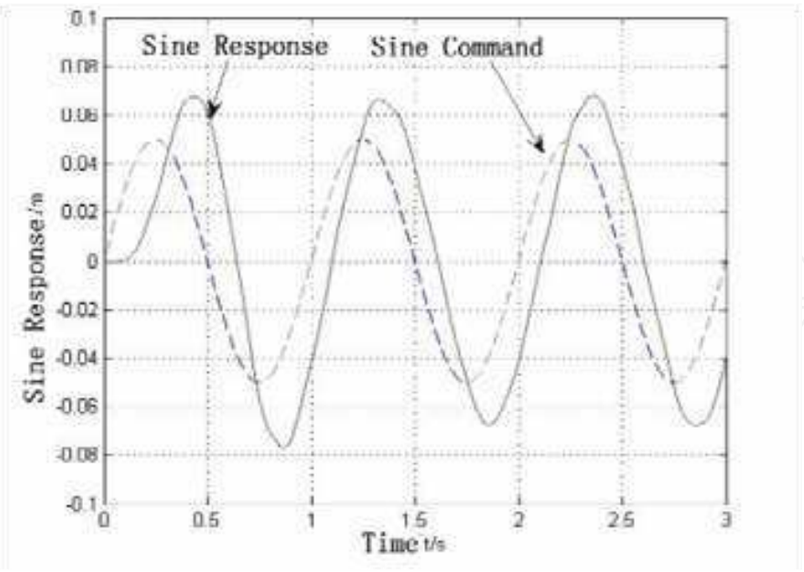

Fig. 19. Experiments Curve of Sine Signal Response

Based on the experiments, the performances of the three different controllers are shown in figure 20.

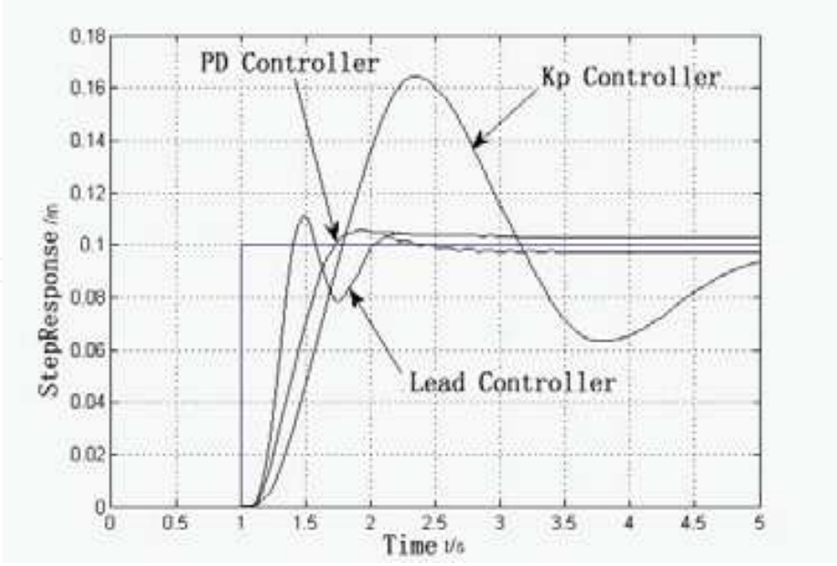

Fig. 20. Comparison of the Experiment results using three different controllers

The following function parameters based on step response are obtained from figure 20.

System Function Value	ising Time/s	ransit Time/s	Surpass Amounts	teady Error	Oscillation Number
LagLeadcontroller	.37	.96	11.5%	%	2
KD Controller	.62	.97	6%	%	1
Kp Controller	.73	.9	64%	%	3

Table 1. Comparison of Function Values from Experiments using three different controllers

The functional parameters shows that the controller designed by the method based on the experimental step response of the closed-loop system improves the system performance a lot, even much better than the proportion differential controller, while the design process is far simple than the design of PD controller.

2.3 Energy harvest EHMD control system

In the following figure 21, the main parts of the innovative EHMD system and their relations were illustrated, respectively. The EHMD system can be divided into the following parts: TMD subsystem with energy dissipating and recycling functions, power module which can preserve and release electrical energy, EMD subsystem which is directly driven by electro-magnetic force. To be specific, TMD damper is replaced by coils embedded fly-wheels combined with high-power batteries, EMD active force is realized using soft magnetic material actuator and high-power capacitor; besides, the standard DSP module is incorporated to make up a real-time control system. The fly-wheels is composed of wheel body, reducer or accelerator using gear boxes, energy generating and dissipating coils, high power storage battery and capacitor, electronic and electrical regulator, as well as mechanical couplings and attachments etc. Considering the fly-wheel battery is relatively a matured technique, here the EHMD should be focused on solving its control strategies to realize a reasonable energy preserving-releasing process for structural active control.

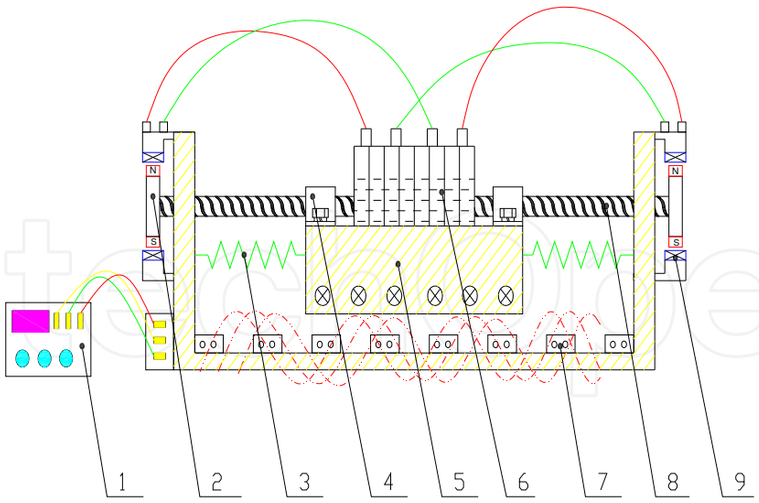

(Note: 1-digital controller, 2-fly-wheel(s), 3-spring element, 4-mechanical couplings, 5-system mass (embedded coils), 6-energy-storing battery, 7-excitation coils, 8-bearings and system rails, 9-permanent magnets)

Fig. 21. Structural integration photos of EHMD system

In the following figure 22, analysis and design procedure of the EHMD system is proposed. First, aiming at the requirement of the specific structure to be controlled, optimal mass ratio, stiffness and damping coefficients, maximum mass stroke and peak control force were calculated, which were set as the hardware standard parameters of the moderate scale EHMD system. Second, applying relevant research results, such as linear motor technique in magneto suspension trains and energy accumulation technologies in fly-wheel batteries etc, key parts of energy recycling, preserving and utilizing for driving EHMD system would be developed. At last, integrating DSP based data acquisition, processing and real-time control modules, the whole experimental EHMD system are fabricated and integrated.

When the structure vibrates, the mass moves driving the couplings rotating which transforms linear motion into rotation, and the embedded coil cut the magnetic field and generates induction currents and stored in the batteries which will be utilized at a

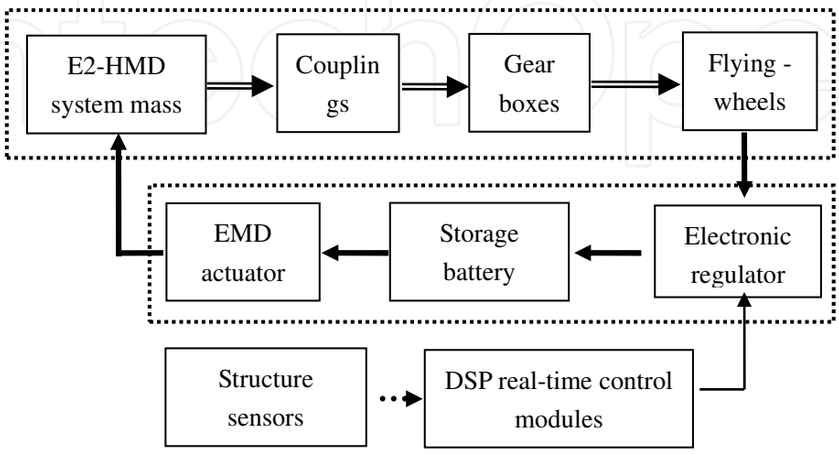

Fig. 22. Structural construction sketch of EHMD system

reasonable occasion. If reducer or accelerator is incorporated into the system, then the efficiency of generating electrical power can be greatly improved, through calculations the optimal gear ratio and damping coefficient can be achieved.
In the following, feasibility of utilizing such kind of EHMD system for suppressing structural vibrations will be considered. Basically, the main problems will be focused on the electrical loops of the system, because the other two major parts will be benefited from AMD and TMD control techniques. Currently, a high-power capacitor can be stored with energy of up to 3MJ, where its energy density will be 1.35kJ / kg and about 1.5kJ / dm^3, thus the mass will be about $2m^3$ and the weight will be 2tons or so, which can power the EMD actuator in continuous working mode for more than 200 seconds. From the data, the EHMD for protection of structural seismic response is absolutely feasible.

3. DDVC based AMD control system

This DDVC based active mass driver control system is proposed for low frequency vibration and motion control, *e.g.* wave induced motion control of offshore platform structures. DDVC (Direct Drive Volume Control) technology comes from the hydraulic industry, which utilizes integrated pump and motor to replace servo valve from traditional hydro cylinders, and to realize such functions as pressure control, speed control and changing working directions etc. DDVC control is also called as valve-less control, which uses servo AC motors driving fixed displacement pumps. DDVC is operated based on regulating rotary speed of pumps rather than changing its flow, and to control actuating speed of actuators. DDVC has been widely researched by institutions from Japan, USA, German, Sweden and China. The most common applications are used in such industries as high-precision forging machinery, ship helms, heavy load casting machineries, printing machines, 6-DOF platforms and rotary tables, 2500 ton inner high pressure shaping machine, operating switch for floodgates etc. Besides, some applications have been proposed for aerospace engineering (also called EHA, Electrical Hydro Actuator) recently because the most attracting advantages of compact volumes, high energy saving efficiencies etc.
Figure 23 shows the photo of one typical DDVC system fabricated by 1st Japan Electric Corporation. DDVC-AMD is an innovative replacement of actuator from traditional hydro cylindrical AMD control system, and figure 24 shows the working principles of such DDVC actuated AMD control system.

Fig. 23. Photo of DDVC driver

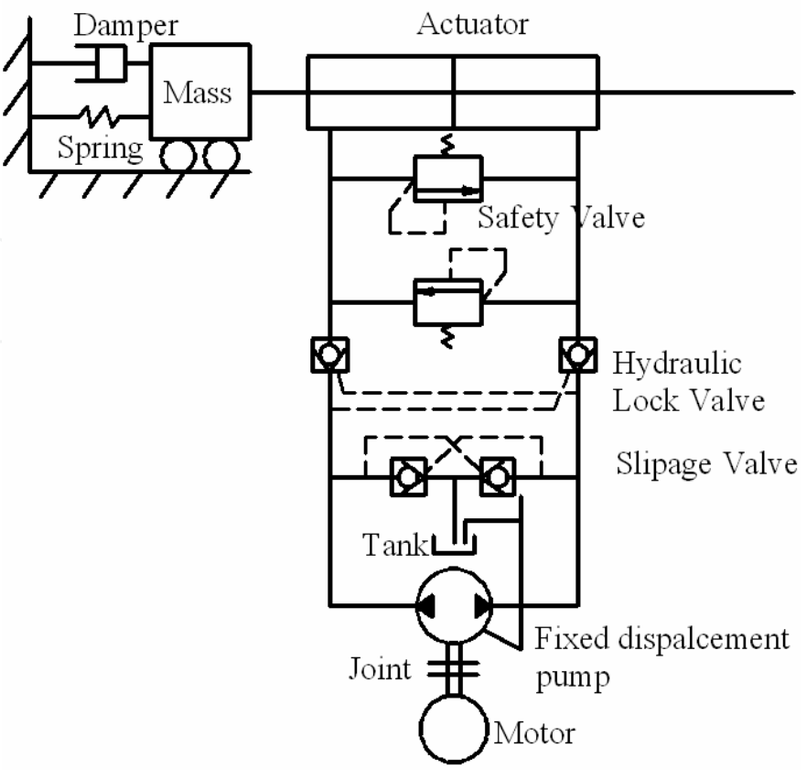

Fig. 24. Principle chart of DDVC-AMD system

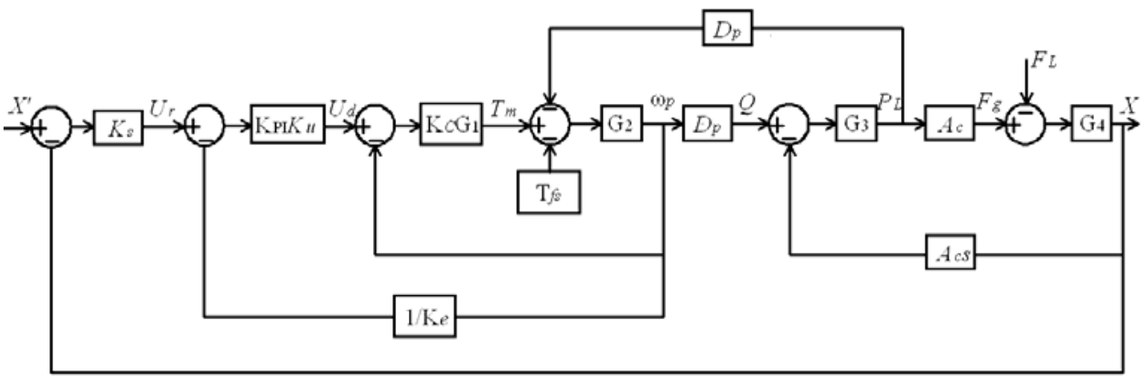

Fig. 25. Simulation block diagram for DDVC-AMD control system

The following section established the formulations for DDVC based AMD control system. Motor control loop, hydraulic power plant and actuation part were studied and numerically validated. As shown in figure 25, Simulink simulation block diagram was used to perform numerical simulations and comparisons on the force-displacement hysteresis loops are given in figure 26. Furthermore, structural seismic response control using DDVC-AMD are numerically studied. Figures 27 to 28 show some preliminary results under Kobe and Hachinohe earthquake excitations, which indicates the feasibility and effectiveness of such system for structural vibration mitigation.

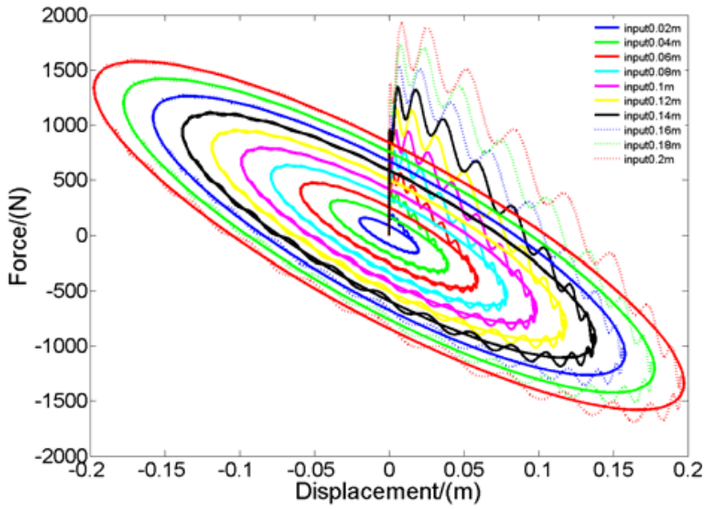

Fig. 26. Hysteresis loops of DDVC-AMD under different loading amplitudes

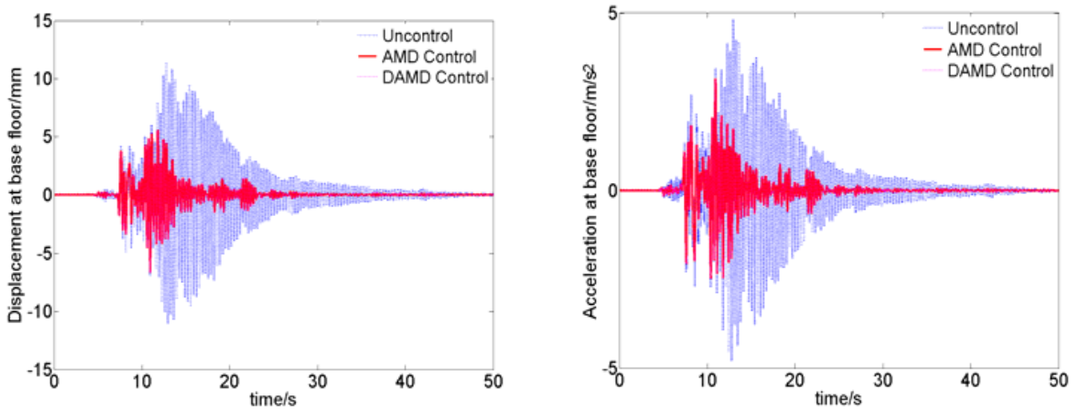

a) Displacement of first floor b) Acceleration of first floor

Fig. 27. Kobe earthquake excitation

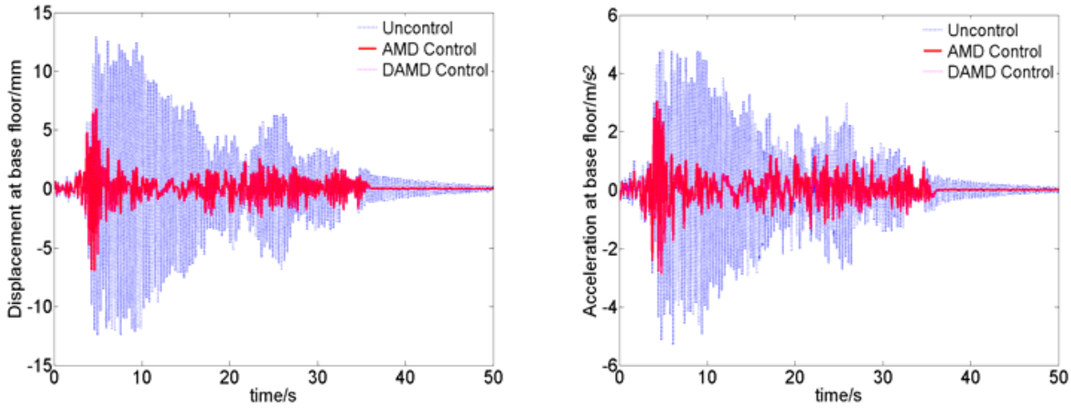

a) Displacement of first floor b) Acceleration of first floor

Fig. 28. Hachinohe earthquake excitation

4. Structural swinging motion and vibration control

Vessel-mounted cranes of heavy lifting and pipeline paving ships are used to construct large scale offshore structures, such as steel jacket platforms and oil-gas transporting pipeline systems etc. Owing to the complicated conditions of ocean environment, the wave-induced ship motion, sometimes wind-wave-current coupling excitations of the crane ship produces large pendulation of hook structure, which causes normal operations of the ship to be suspended and results in economic losses. For example, when the wind speed exceeds 6 degree, the probability of suspended operations will be about 50%, which greatly affects the construction progress.

Based on a large amount of observations on the hook vibration, the pendulation can be divided into two types: in-plain motion and rotary motion with respect to certain axis (namely gyrus motion). After thorough numerical simulations and experimental verifications, the control solution corresponding to each type of the motion is found to be absolutely different.

In the followings, the modeling of two motion modes and the methods of suppressing different types of pendulation of hook structure will be discussed respectively, and eventually be experimentally verified on a scale model structure.

4.1 Theoretical modeling

The calculation sketch of the crane ship can be simplified as a SDOF system, which is represented using a basket model as shown in figure 29, and a passive TMD (Tuned Mass Damper) control system is attached onto the structure. Based on the measurement of the motion of the suspended hook structure, the pendulation could be classified into two modes owing to different relation between suspension points and motion direction as shown in figure 29, where SP stands for "suspension points".

After thorough theoretical analysis and numerical simulations, the two types of motion is found to be absolute different, and the Lagrange's equation is introduced to model each motion mode respectively. As shown in figure 30, to quantity compare the differences, the hook is simplified as a bar with two masses on each end, besides the TMD system is simplified as a spring-mass second system. Using x stands for mass strokes of TMD system,

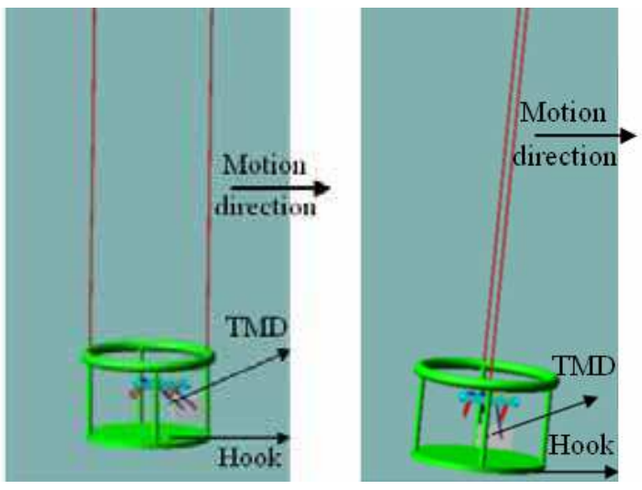

Fig. 29. Suspension points and motion directions

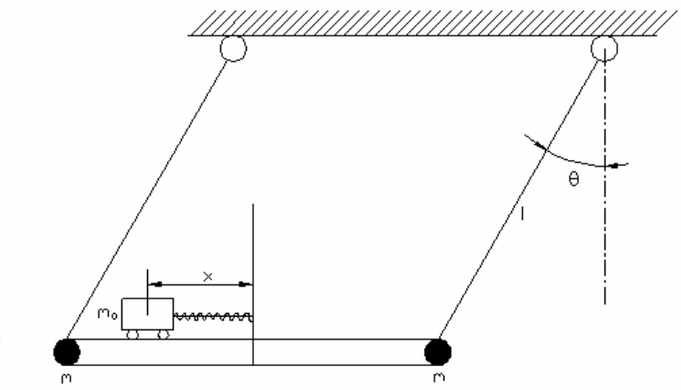

(a) In-plain motion

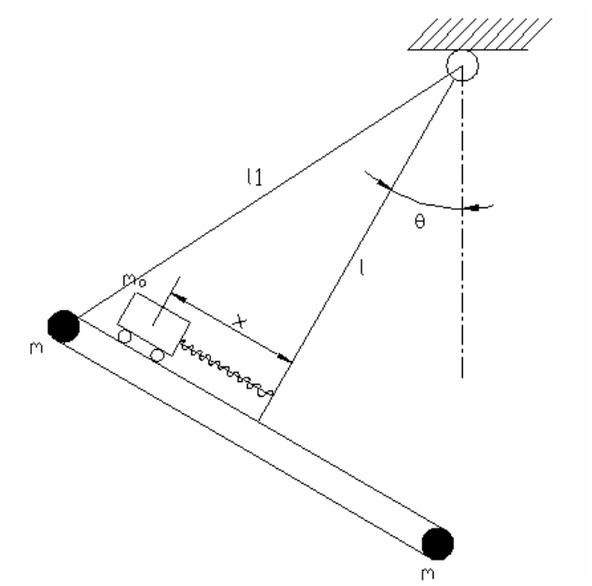

(b) Rotary motion

Fig. 30. Typical motion modes

l stands for the length of suspension cable, θ stands for pendulation angle with respect to vertical direction, m stands for one half of the mass of hook structure, m_a stands for mass of TMD control system.

The whole system shown in figure 30(a) has the following kinetic energy and potential energy expressions:

$$T = ml\dot{\theta}^2 + \frac{1}{2}m_a l\dot{\theta}^2 + \frac{1}{2}m_a\dot{x}^2 + m_a l\dot{x}\dot{\theta}\cos\theta \tag{12}$$

$$V = 2mgl\left(1-\cos\theta\right) + m_a gl\left(1-\cos\theta\right) + \frac{1}{2}kx^2 \tag{13}$$

Using Lagrange's formulation, $L = T - V$, $\frac{d}{dt}\left(\frac{\partial L}{\partial \dot{x}}\right) - \frac{\partial L}{\partial x} = 0$ and $\frac{d}{dt}\left(\frac{\partial L}{\partial \dot{\theta}}\right) - \frac{\partial L}{\partial \theta} = 0$, we have

$$\ddot{x} + \frac{k}{m_a} x = l\dot{\theta}^2 \sin\theta - l\ddot{\theta}\cos\theta \tag{14}$$

$$2ml^2\ddot{\theta} + m_a l^2\ddot{\theta} + m_a l\ddot{x}\cos\theta + 2mgl\sin\theta + m_a gl\sin\theta = 0 \tag{15}$$

Equation (14) gives the solution of TMD mass strokes relative to the main structure, and equation (15) is the standard formula of simple pendulum structure.
For comparison, the kinetic energy and potential energy of the system shown in figure 30(b) has the following expressions:

$$T = ml_1{}^2\dot{\theta}^2 + \frac{1}{2}m_a\dot{x}^2 + \frac{1}{2}m_a\left(l^2 + x^2\right)\dot{\theta}^2 + m_a xl\dot{\theta} \tag{16}$$

$$V = 2mgl\left(1 - \cos\theta\right) + m_a g\left(l - l\cos\theta + x\sin\theta\right) + \frac{1}{2}kx^2 \tag{17}$$

Where l_1 is the distance between suspension point and concentrated mass of the suspended structure. Similarly, using Lagrange's formulation, the equation of motion can be achieved as

$$\ddot{x} + \frac{k}{m_a} x = x\dot{\theta}^2 - l\ddot{\theta} - g\sin\theta \tag{18}$$

$$\begin{aligned} &2ml_1{}^2\ddot{\theta} + m_a\left(l^2 + x^2\right)\ddot{\theta} + 2m_a x\dot{x}\dot{\theta} + m_a l\ddot{x} + \\ &2mgl\sin\theta + m_a gl\sin\theta + m_a gx\cos\theta = 0 \end{aligned} \tag{19}$$

4.2 Numerical simulation

Assuming the system parameters are m=5kg, ma=0.5kg and l=10m, imposing an initial kinetic energy on the suspended structure shown in figure 30(a) and the dynamical response of the system is listed in the figure 31.
Here assuming there is no damping existed in the TMD system, thus the vibration of the system will not be suppressed, and energy exchanges between the TMD control system and the main structure, as shown in figure 31(a) and 31(b). In figure 31, the unified force is defined as the sum of the two items in the right hand side of equation (14). From the definition we can see that such kind of unified force is independent of mass strokes x, which was also verified by the simulation results shown above. From both the figures and the equations, we can see that the unified force of the TMD system is proportional to the vibration amplitude of the structure, which is equals to the control force which is imposed onto the main structure. Thus the TMD system behaves like a closed-loop feedback control system of the structure (Zhang *etal*., 2006).
On the other hand, equation (18) gives the equation of TMD mass in the second suspension case, where the last two items are the ideal motion equation of the simple pendulum system. The control force of TMD system is shown to be dependent on the product of x times angular velocity. After a lot of simulations, the mass stroke is shown to be very small, which can not provides sufficient control force to suppress the structural vibrations. Moreover, the

control effectiveness is also affected by the initial phase lags between TMD mass and the hook displacement. As a result, traditional TMD system will lose its effects during the rotary motion mode.

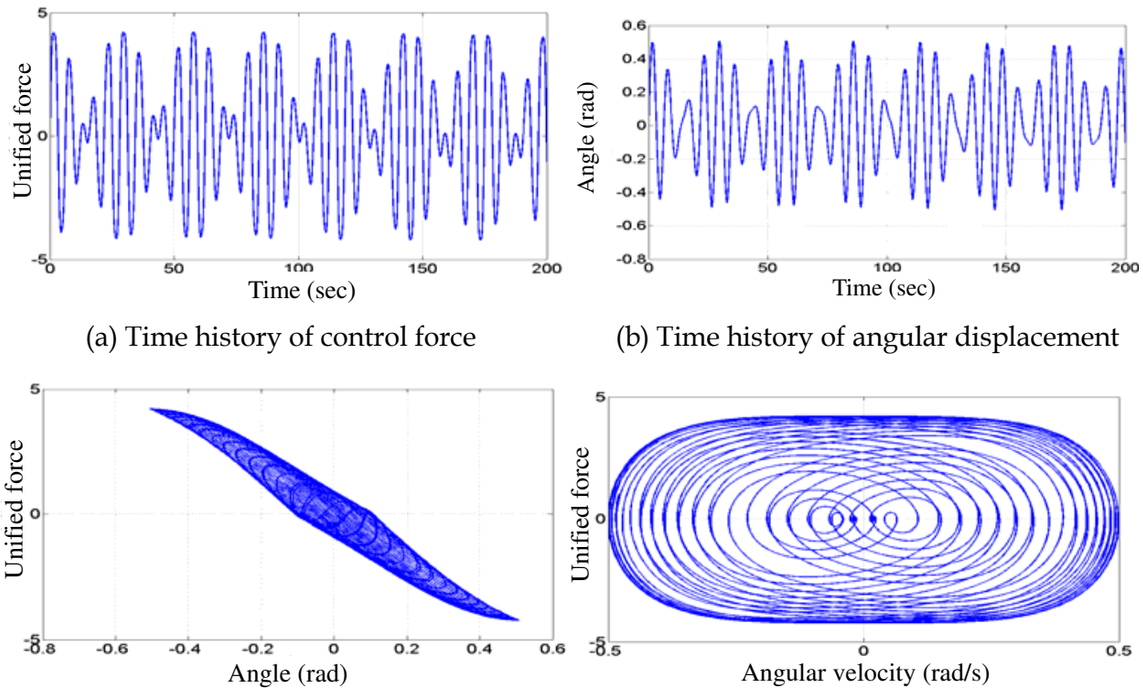

(a) Time history of control force (b) Time history of angular displacement

(c) Hysteresis loop of force-displacement (d) Hysteresis loop of force-velocity

Fig. 31. Numerical simulation responses of in-plain vibration mode

4.3 Solutions for rotary and swinging motion control

For the rotary motion mode, which is exactly similar to the gyrus motion or swing vibration of a simple pendulum, the gravity acceleration plays both as disturbance force and restoring force at the same time, thus the ability of the traditional in-plain control device is of no effect any longer, and innovative mechanism or special device, which can exert control torques to suppress such gyrus motion should be developed.

Taking a simple pendulum system for example, the suspended structure and the gyrus motion control system is shown in figure 32, where m_0 is the mass of hook structure, l_0 is the length of suspension cable, r is the radius of fly-wheel, for simplification, m is the representative value of half mass of the fly-wheel, θ and φ are angle of wheel rotation and vertical direction respectively.

Kinetic and potential energy of the simple pendulum and rotary control system shown in figure 32 are given below, where k_t is the stiffness coefficient of torsion spring.

$$T = \frac{1}{2}(m_0 + m_a)l_0^2\dot{\varphi}^2 + m_a r^2\dot{\theta}^2 \tag{20}$$

$$V = (m_0 + 2m_a)gl_0(1 - \cos\varphi) + \frac{1}{2}k_t(\theta - \varphi)^2 \tag{21}$$

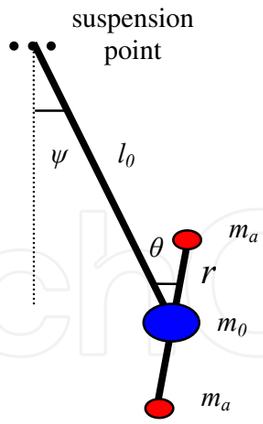

Fig. 32. Computational sketch of rotary motion

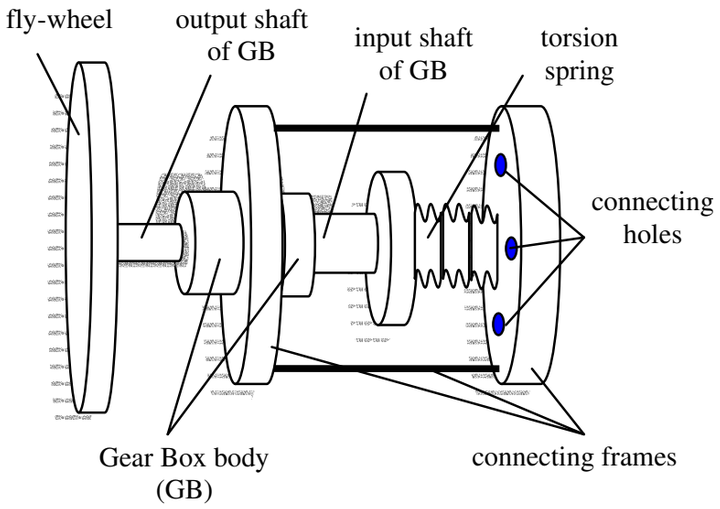

Fig. 33. Numerical simulation responses of in-plain vibration mode

Using Lagrange's principal, the system equations of motion can be achieved as

$$\left(m_0 + 2m_a\right) l_0^{\,2}\ddot{\phi} + \left(m_0 + 2m_a\right) g l_0 \sin\phi - k_t\left(\phi - \theta\right) = 0 \tag{22}$$

$$2m_a r^2\ddot{\theta} + k_t\left(\theta - \varphi\right) = 0 \tag{23}$$

In order to control the rotary motion, the control system must be able to rotate relative to the pendulation of the hook structure. The innovative tuned torsion inertia damper system is composed of torsion spring element, fly-wheel, gear boxes and necessary connecting accessories is developed and its main structure is shown in figure 33. If the reducer gear box is introduced, then the volume of the whole rotary control system can be greatly reduced, and the rotation inertia of the control system can be increased by i^2 times, where i is the gear ratio. The intrinsic characteristic of such an innovative rotary control system is to use high rotation speed to make up for the smaller physical rotation inertia indeed. After incorporating gear box device, equations (22) and (23) can be rewritten as

$$\ddot{\phi} = \frac{1}{(m_0 + m_1 + m_2)l_0^2}[-(m_0 + m_1 + m_2)gl_0 \sin\varphi + k_t(\theta - \varphi)] \tag{24}$$

$$\ddot{\theta} = \frac{1}{(m_1 r_1^2 + i^2 m_2 r_2^2)}[-k_t(\theta - \varphi)] \tag{25}$$

Where m_1 is mass of the input shaft (low speed end) of reducer GB box and r_1 is the rotation inertia radius of m_1, m_2 is the mass of output shaft (high speed end) of reducer GB box and r_1 is the corresponding rotation inertia radius.

4.4 Innovative TRID control system

TRID system, as shown in figure 34, was composed of a torsion spring, with the stiffness k_t, and a cricoid mass, with the mass m and the radius r, so the rotation inertia can be expressed as $J_a = mr^2$.

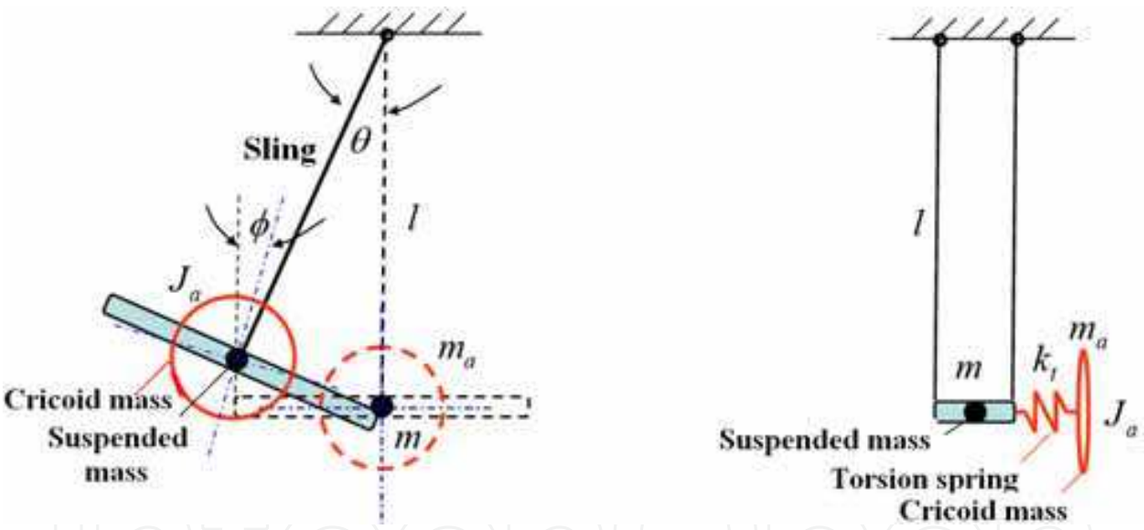

(a) Front view (b) Side view

Fig. 34. Pendulum-TRID system

Based on the Lagrange principle, the differential equation of free pendular vibration with TRID system is:

$$\begin{cases} (m + m_a)l^2\ddot{\theta} + (m + m_a)gl\sin\theta - c_t(\dot{\phi} - \dot{\theta}) - k_t(\phi - \theta) = 0 \\ J_a\ddot{\phi} + c_t(\dot{\phi} - \dot{\theta}) + k_t(\phi - \theta) = 0 \end{cases}$$

Where: θ denotes the angle of the pendulum, ϕ denotes the angle of the torsion spring. The following are some primary simulation results:

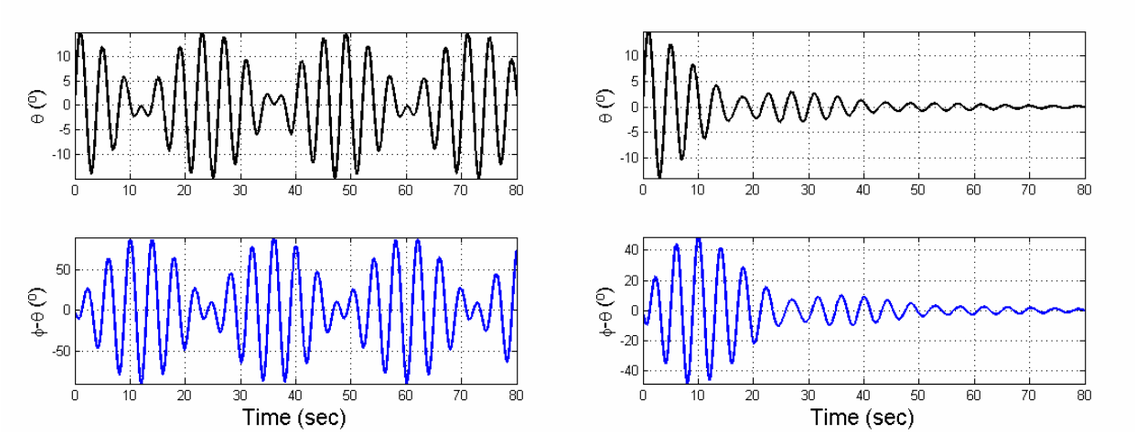

(a) No damping ($c_t = 0$) (b) Optimal damping

Fig. 35. Free pendular vibration controlled with TRID system

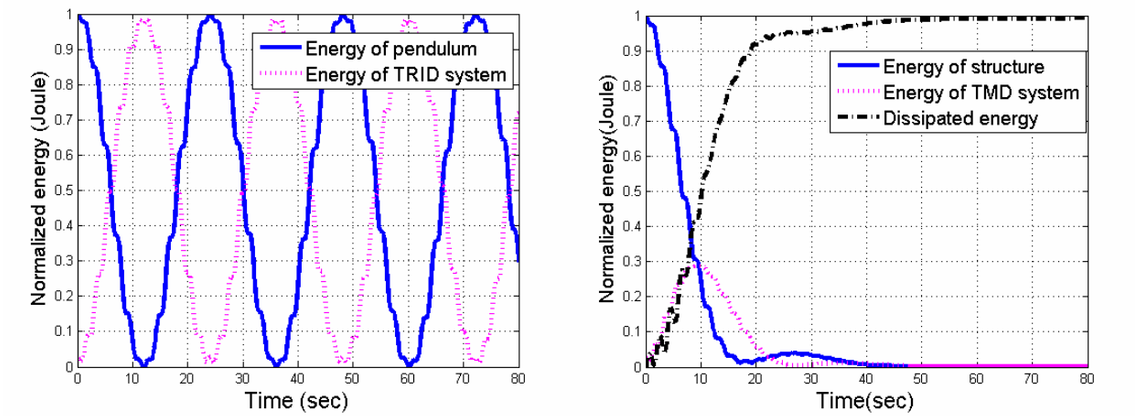

(a) No damping ($c_t = 0$) (b) Optimal damping

Fig. 36. Energy transmission and dissipation of pendulum-TRID system

Figure 35 shows that the TRID control system was effective for the control of free pendular vibration. And figure 36(a) shows the energy transmission between the pendulum and the TRID system without damping in the TRID system. If there is an appropriate damping in the TRID system, the energy transmitted to the TRID system will be dissipated gradually. Thus, the total energy of the pendulum-TRID system decays and the pendular vibration is controlled finally.

4.4.1 Forced pendular vibration control

For excited pendular vibration with displacement excitation at the suspended points, the differential equation is:

$$\begin{cases} (m+m_a)l^2\ddot{\theta} + (m+m_a)gl\sin\theta - c_t\left(\dot{\phi}-\dot{\theta}\right) - k_t\left(\phi-\theta\right) = -(m+m_a)l\ddot{x}\cos\theta \\ J_a\ddot{\phi} + c_t\left(\dot{\phi}-\dot{\theta}\right) + k_t\left(\phi-\theta\right) = 0 \end{cases}$$

Where: $\ddot{x}$ denotes the acceleration of the moving suspended point of the structure.
And some numerical results of excited pendular vibration control are given in figure 37.

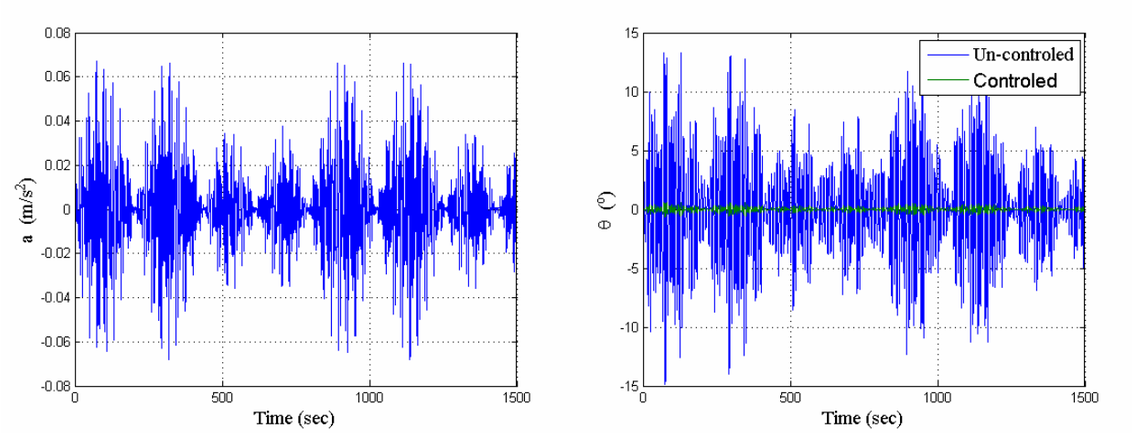

(a) The acceleration of the upper point: $\ddot{x}$ (b) The angle of the pendular vibration

(c) The angle of the inertia (d) The angle of the controlled pendular vibration

Fig. 37. Forced pendular vibration controlled with TRID system

4.4.2 Experimental investigations

A series of experiments of both free pendular vibration and harmonic excited pendular vibration with TRID system were carried out. The experimental setup and some results are shown in figure 38 and figure 39, respectively.
From figure 39, the test results as well as the simulation results show that the TRID system is effective in suppressing the pendular vibration of both free and forced vibrations.

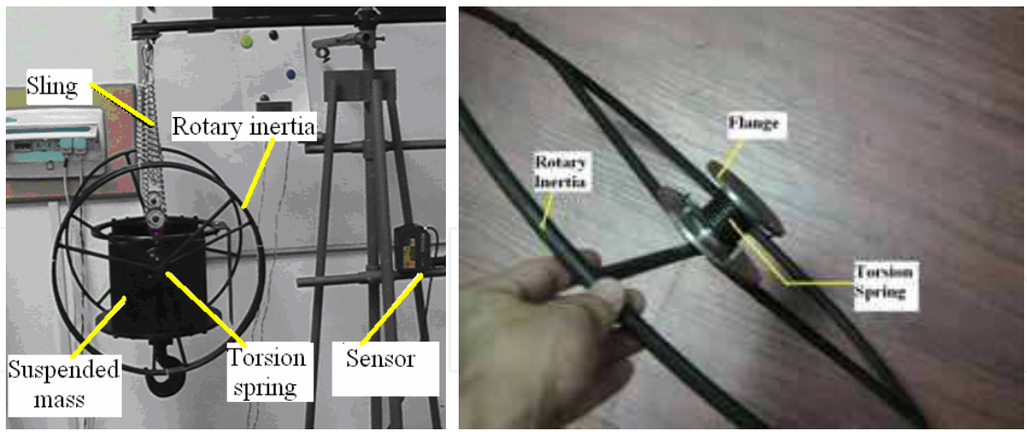

(a) Pendulum-TRID system (b) The model of TRID system

Fig. 38. The equipments of the experiments

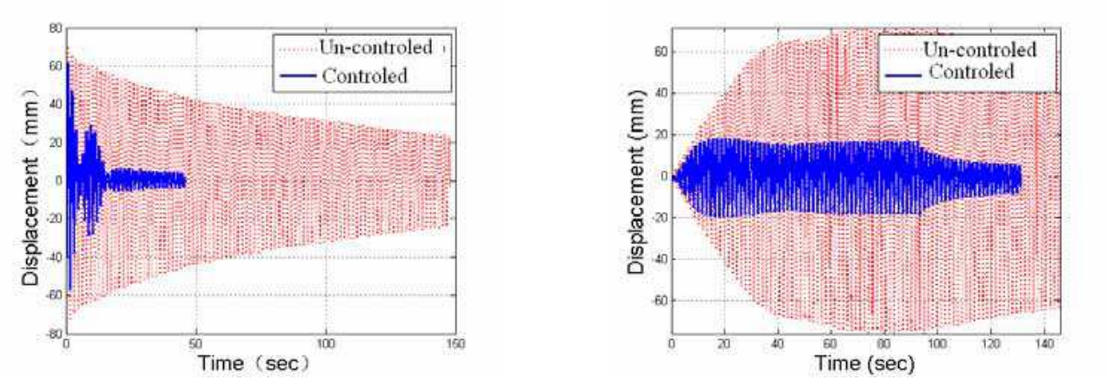

(a) Free pendular vibration control (b)Harmonic excited pendular vibration control

Fig. 39. Pendular vibration controlled with TRID system

4.4.3 Parameter optimization of TRID control system

The effect of TRID system mainly depends on its frequency tuning ratio and damping ratio. Based on a lot of numerical simulations, the following results were obtained:

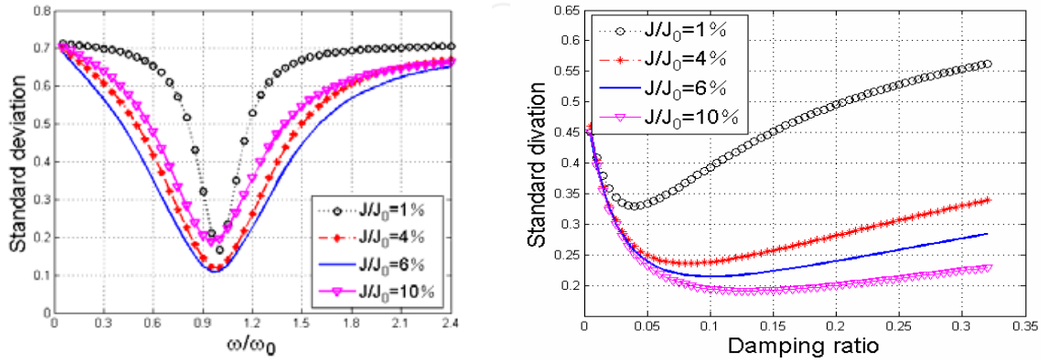

(a) Tuning ratio (b) Damping ratio

Fig. 40. Impact of the main parameters of TRID control system

Figure 40(a) shows that the TRID system have the best performance when the frequency ratio is set to 1.0 or so. Beyond that range, the TRID system loses its effectiveness quickly. Figure 40(b) shows the damping ratio impact of TRID system under different inertia ratios. The simulation results indicate that when the design of TRID system is being considered, the intersect influence of parameters must be addressed.

4.5 Preliminary results on TRID control system

This part studies an innovative passive control system for rotary motion control of suspended hook structures, and main conclusions are achieved as:

1. Gravity acceleration is the disturbance effect on the in-plain motion of the suspension hook structure, on the other hand, it plays as disturbance as well as restoring force in the rotation mode of the structure.
2. According to different motion types, traditional TMD system can be used to control the in-plain motion, however, only the tuned torsion inertia damper is shown to be feasible for reducing the rotary (gyrus) motion.
3. For the miniaturization of the innovative rotary control system, the reducer gear box is introduced, which compensates system rotation inertias at the cost of high rotation speed. Through model test, the control system is proven to be feasible and effective.

5. Force characteristics of AMD control system

5.1 Background

The wind-induced vibration control problem of the Melbourne Benchmark building has attracted much research concern in the past eight years, and a lot of control schemes either in control algorithms or in physical control systems have been proposed by researchers all over the world (Yang *etal.*, 1998, 2004; Ricciardelli *etal.*, 2003; Samali *etal.*, 2004). Ou studied the structural interbedded active control scheme for the Benchmark problem, where the active control force of the actuators were found to be possessing the damping force behavior (Ou, 2003), which indicated that all the active actuators can be replaced by semi-active devices or even passive viscous damping devices. As a comparison, after a lot of numerical analysis, Zhang *etal.* (Zhang *etal.,* 2004) disclosed that the active force of AMD control system doesn't possess damping behavior, which resulted in the actuators of AMD control system can not be replaced by any semi-active devices. On the other hand, after the more than 30 years development of structural active control research (Ou, 2003), the Active Mass Driver/Damper (AMD) control, with the better control effect and cheaper control cost, has taken the lead in various active control occasions, becoming the most extensively used and researched control method in practical applications (Soong, 1990; Housner *etal.*, 1997; Spencer *etal.*, 1997; Ou, 2003). Besides, several important journals in civil engineering field, such as ASCE Journal of Engineering Mechanics (issue *4th*, in 2004), ASCE Journal of Structural Engineering (issue *7th*, in 2003), Earthquake Engineering and Structural Dynamics (issue *11th*, in 2001 and issue *11th*, in 1998), reviewed the-state-of-the-art in research and engineering applications of semi-active control and active control, especially AMD control. In addition, Spencer and Nagarajaiah (2003) systematically overviewed the applications of active control in civil engineering. Up to date, more than 50 high-rising buildings, television towers and about 15 large-scale bridge towers have been equipped with AMD control systems for reducing wind-induced vibration or earthquake-induced vibration of the structure. As a result, aiming at the above problem, some researchers have

made some studies on the intrinsic characteristic of active control force of different schemes (Horvat *etal.*, 1983; Mita *etal.*, 1992; Pinkaew *etal.*, 2001; Ou *etal.*, 2004; Zhang *etal.*, 2004).
As a continued study, this part is focused on making a systematical comparison for different control schemes under the background of the Benchmark control problem, in order to disclose what are the intrinsic differences for each control scheme and relative advantages as well as restrictions of each control scheme. However the present standard solution of AMD control proposed by Yang *etal.* (2004) has already been widely accepted from all over the world, which is based on a reduced order of structural model, some changes must be conducted to the existing control scheme first in order to achieve at the same level for comparison of different active control schemes.

5.2 Comparisons on analysis of AMD control

Yang *etal.* (2004) proposed the AMD control scheme, where the mass is 500 ton, which accounts for nearly 0.32% of the total structural weight. Besides, a standard program based on Matlab was also incorporated. Under the input of first 900 seconds of the wind load accquired by wind tunnel test (Samali *et al.*, 2004), the results of standard solution are given in table 2.

Items	Peak reduction (%)		RMS reduction (%)		Control cost	
	Displacement	Acceleration	Displacement	Acceleration	Control force (kN)	Mass stroke (cm)
Values	28.3	49	42.2	49.7	118	73.3

Table 2. Standard solution of AMD control for the wind-excited Benchmark problem

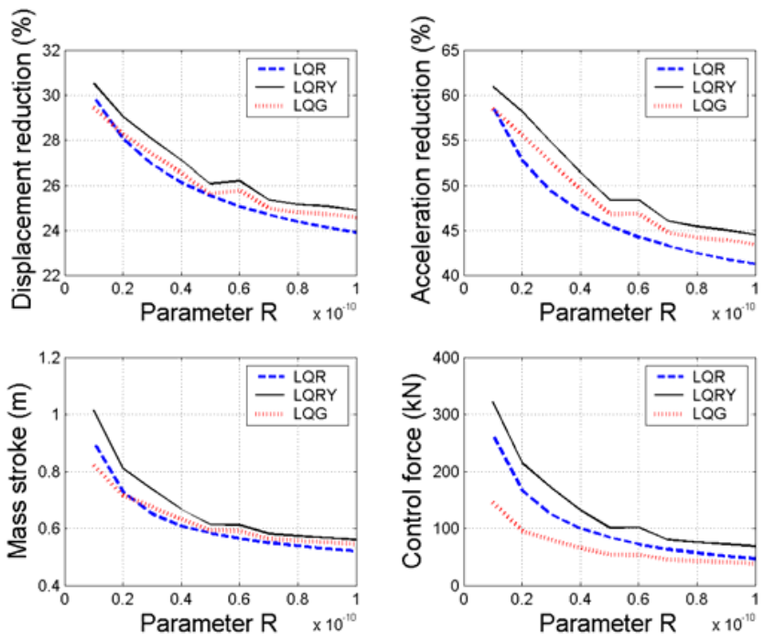

Fig. 41. Comparison of AMD control effect based on non-reduced model under three control algorithms

Here the control analysis was conducted on a reduced order structural model, however, in this part all the three control schemes should be compared on a same model, after a thorough comparison on the impact of order reduction on the Benchmark control problem, the non-reduced model, 76DOFs structure, is found to be the most appropriate (Zhang, 2005). In order to exclude the possible influence caused by control algorithms and their weight parameters, the proposed AMD control scheme deals with three independent control algorithms respectively, classical Linear Quadratic Regulator (LQR), output based optimal control (named as LQRY) and Linear Quadratic Gauss (LQG) control. Figure 41 shows the peak response of the top structural floor under the three algorithms, where all weight parameters in Q matrix of LQR are set to be unit, except parameters corresponding to the state of mass are set to be zero.

In addition, quantitative results of the proposed AMD control scheme are given in the following table, which are comparative with the standard Benchmark solution.

Items	Peak reduction (%)		RMS reduction (%)		Control cost	
	Displacement	Acceleration	Displacement	Acceleration	Control force (kN)	Mass stroke (cm)
Control results	24~30	42~58	36~44	47~60	50~270	55~90

(RMS: root mean square value.)

Table 3. Solution of AMD control based on non-reduced order structure

5.3 Structural interbedded active control

Structural interbedded active control (STI) is to add actuators into the adjacent structural inter-storeys, such as active brace systems (ABS) or active tendon systems (ATS), where active force is being directly exerted onto the structural floors or column-beam joints. However, for numerical analysis purpose, the control force and its counter force should be both considered at the same time from the equation of motion of the system. Furthermore, if every actuator takes the same value, then owing to the quits effect, the ultimate situation is equal to add two forces with opposite direction, one at the bottom and the other at the top, which equals to the effect of an active moment. On the other hand, AMD control system utilizes the mass as supporting point for the counter force, so it is absolutely different from STI control during calculation. Figure 42 shows the conception comparison between those two control schemes.

5.3.1 Comparison between STI control and AMD control

The optimization placement of actuators for STI control scheme is not the concerned question here, so we assume that the structure be controlled by placing actuators at each floor throughout the building. Zhang *etal*. (2005) have made a thorough comparison on control algorithms as well as impact of weight parameters, and here a representative case is chosen with its settings of control parameters based on LQR algorithm given in table 4, which is going to be used for comparison with AMD control scheme.

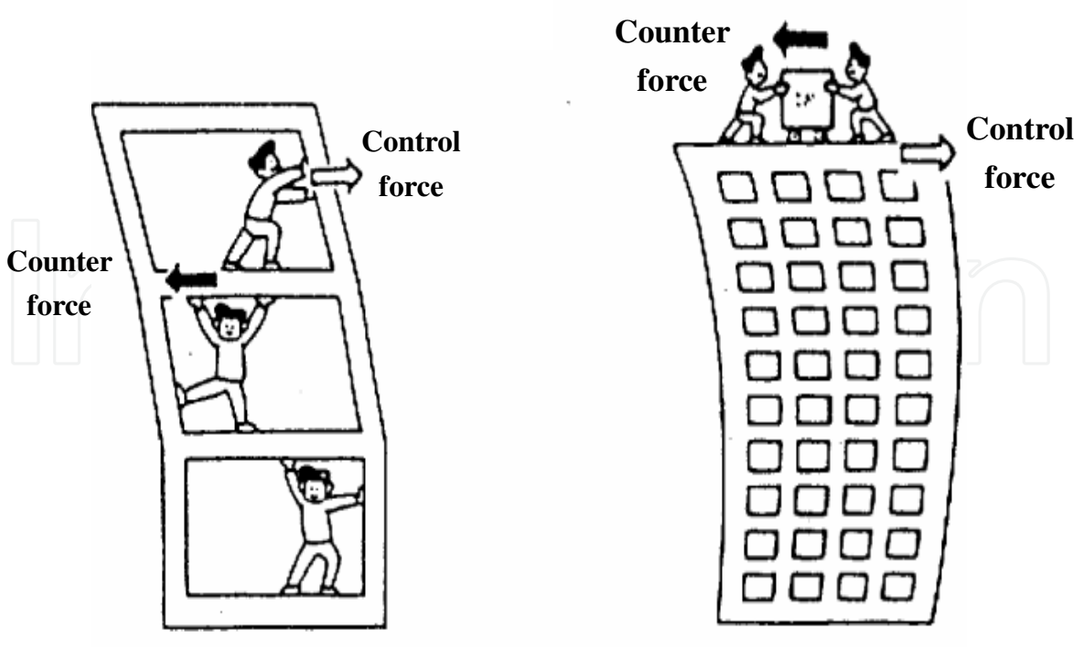

(a) STI control (b) AMD control

Fig. 42. Sketch of control force and counter force between active control system and structure

Parameter	AMD control	STI control
Q matrix	$\begin{bmatrix} [I]_{76\times76} & & \\ & 0 & \\ & & [I]_{76\times76} \\ & & & 0 \end{bmatrix}$	$[I]_{152\times152}$
R matrix	$r = 1\times10^{-11}$	$1\times10^{-13}\times[I]_{76\times76}\times\sqrt{\Phi_1}$

(Note: Φ_1 is the first column vector of the structural flexibility matrix; $[I]_{n\times n}$ is a unit matrix with the dimension of $n\times n$.)

Table 4. Parameters of LQR control algorithm for AMD and STI control schemes

Under the above settings, the structural response is calculated to be controlled within the same range for the two control schemes as shown in figure 43.

Figure 44 shows the control forces corresponding to the above two schemes. First the left two figures show two time histories of control force for comparison, the upper is the STI control force at the 60th floor and the lower is the AMD control force. Besides, the right figure shows the peak and RMS control force of each floor of the STI control scheme, where the peak values falls between 400kN to 500kN, and the RMS values all exceed 100kN. Basically we can find that STI control is achieving the comparative control performance at the cost of tens times of the AMD control. The specific results for the two control schemes are: 1) For AMD control, the peak value is 265kN and the RMS value is 63.5kN; 2) For the STI control, it needs 76 actuators, and the peak forces range from 372kN to 527kN with the average is 438kN, besides, the average RMS force is 125kN. As a result, the STI control is

shown to be at the cost of 125~150 times of AMD control to get the similar performance, therefore the AMD control scheme is shown to be economical and advantageous for the Benchmark problem.

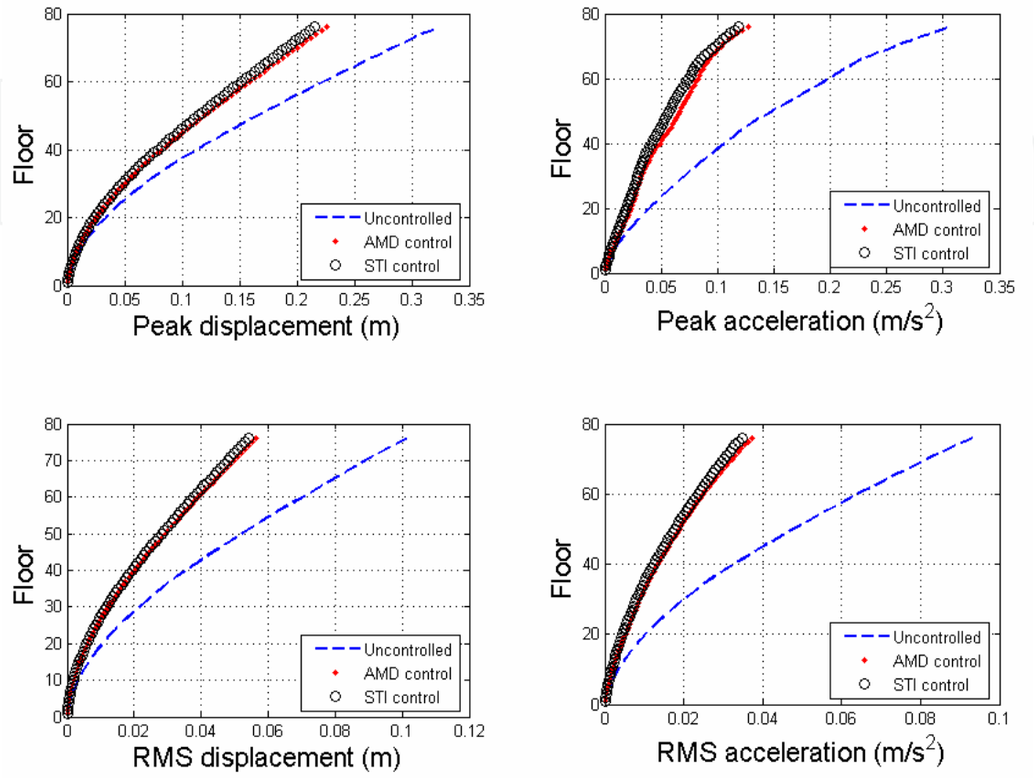

Fig. 43. Controlled response of the structure under AMD control and STI control

In addition, Ou (2003) has put forward another STI control scheme, where 20 actuators are employed and they were placed at every other 3 floors from the bottom floor to the top floor. If the control goal was chosen for 33.5% reduction in peak structural displacement and 46.8% reduction in acceleration, then the corresponding control forces of each actuator should be from 100kN to 1500kN. In the following table, the results of the above two STI control schemes as well as AMD control scheme are summarized.

Control results	Reduction of displacement (%)		Reduction of acceleration (%)		Actuator devices	
	Peak value	RMS value	Peak value	RMS value	Peak force (kN)	Quantity
AMD control	30.0	43.3	58.7	59.9	265	1
STI control (in this part)	33.2	46.5	61.3	62.7	372~527	76
STI control (Ou, 2003)	33.5	-	46.8	-	110~1500	20

Table 5. Comparison of AMD control scheme with STI control scheme

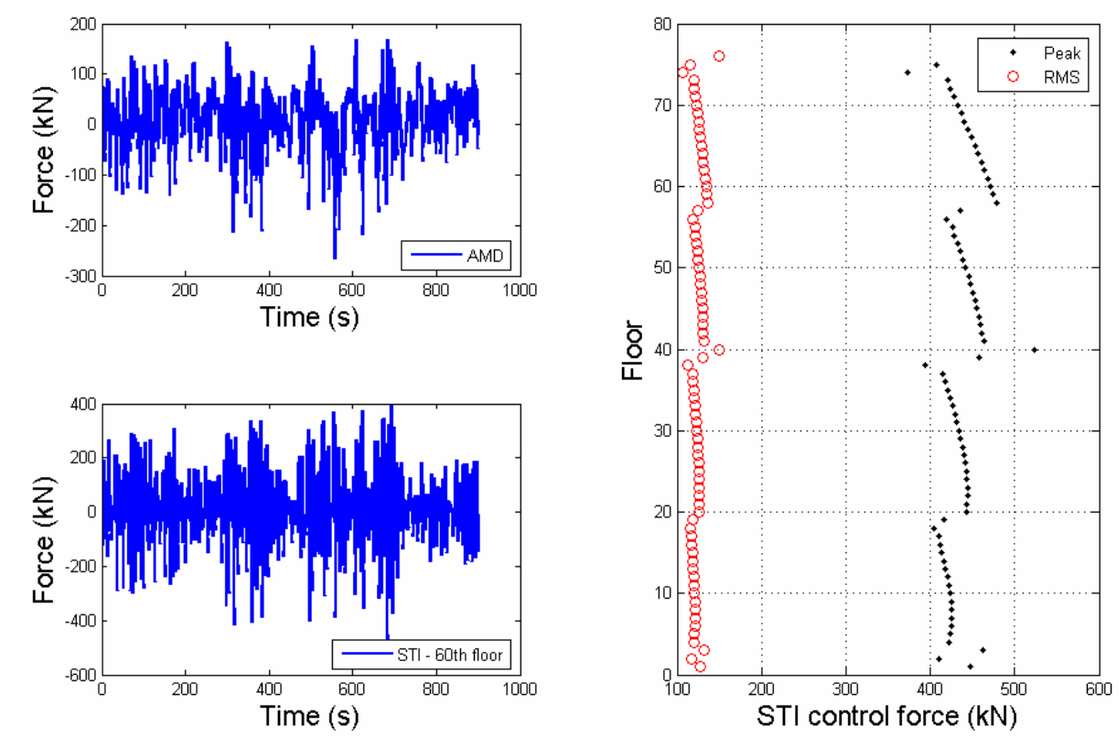

Fig. 44. Comparison of STI control force with AMD control force

From the results above, the AMD control is shown to be more superior and economical than STI control for the Benchmark building.

5.3.2 Characteristic of control force of STI control scheme

So far, the STI control is shown to be more consumptive than AMD control, for example the total control force is about 125 times of that of AMD control, while achieving at the comparative performance. The reason mainly comes from the quits effect between control force and counter force as shown in figure 42, therefore, it is not effective to place pure active actuators at inter-storeys for vibration control of the structure.

Then what are the advantages for STI control, the following sections will focus on the analysis of characteristic of active force, which will show that the active force is purely damping force and can be replaced by semi-active devices completely.

Ou (2003) put forward a set of indices denoting the relationship between control force and relative velocity of actuator. For supplementation, the following three sets of indices are defined as

Index of relationship between active force and relative velocity

$$u^*_i(t) = -\mathrm{sgn}(\dot{x}_i u_i)\left|u_i(t)\right| \tag{26}$$

$$\gamma_{1,i} = \frac{\int_0^{\mathrm{T}} \mathrm{H}(-\dot{x}_i u_i) u^*_i(t)dt}{\int_0^{\mathrm{T}} \left|u_i(t)\right| dt} \tag{27}$$

Where i is the number of floor on which the actuator is being installed, u_i is the control force of the corresponding actuator, $\dot{x}_i$ is the interbedded velocity, T is the time duration, for example the total length of time for analysis; sgn(·) and H(·) are sign function and unit step function respectively.

$$\mathrm{sgn}(x)=\begin{cases}1 & x\geq 0\\ -1 & x<0\end{cases};\ \mathrm{H}(x)=\begin{cases}1 & x\geq 0\\ 0 & x<0\end{cases} \tag{28}$$

Equation (26) defines a virtual time history of the active control force, where positive values of $u^*{}_i(t_j)$ stand for the force $u_i(t_j)$ being opposite to actuator velocity $\dot{x}_i(t_j)$ at time t_j, whereas, negative values stand for the force being in the same direction with velocity. Therefore, equation (27) defines the proportional factor of how much active force is being opposite to the relative velocity of actuator. Figure 45 shows the time history of virtual control force at 60*th* floor corresponding to equation (26).

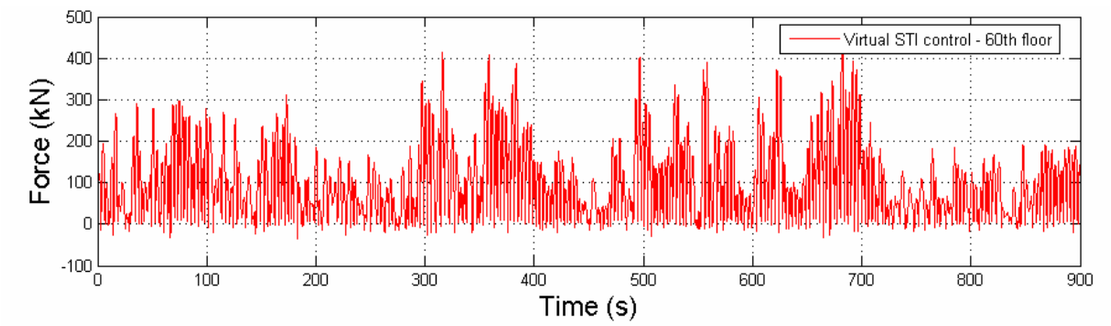

Fig. 45. Virtual time history of STI control force

It can be seen from figure 45 that a large amount of interbedded active control force is being in opposite direction with velocity. For comparison, figure 46 shows the time history of AMD control force after similar transformation, where the direction characteristic of force can't be easily seen. As a result, the two types of forces are different from each other for AMD control and STI control.

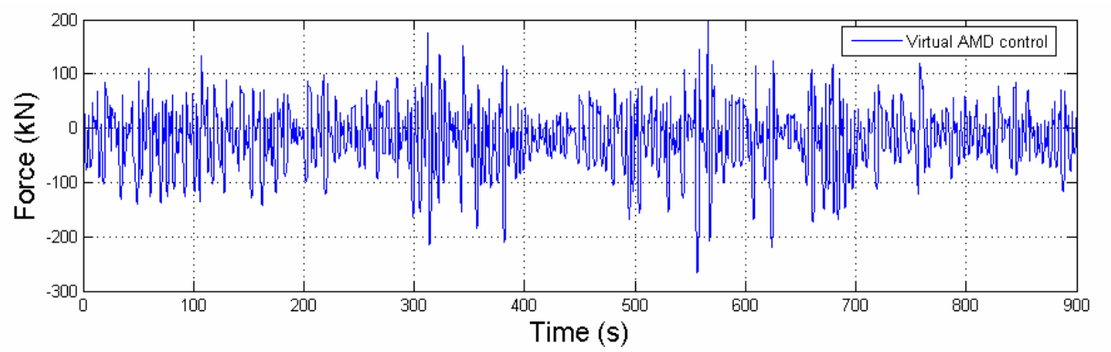

Fig. 46. Virtual time history of AMD control force

Index of relationship between active force with velocity and displacement

$$u^{**}{}_i(t)=-\mathrm{H}(x_i\dot{x}_i)\,\mathrm{sgn}(\dot{x}_i u_i)\left|u_i(t)\right| \tag{29}$$

$$\gamma_{2,i} = \frac{\int_0^{\mathrm{T}} \mathrm{H}(-\dot{x}_i u_i) u^{**}{}_i(t) dt}{\int_0^{\mathrm{T}} |u_i(t)| dt} \tag{30}$$

Where x_i is the interbedded displacement of *ith* floor.
Here equation (29) defines a virtual time history of active control force, where positive values of $u^{**}{}_i(t_j)$ stand for the force $u_i(t_j)$ being opposite to its velocity $\dot{x}_i(t_j)$ during the actuator vibrating against its equilibrium position. Accordingly, equation (30) defines the proportional factor of how much active force is being opposite to its relative velocity during that period.
Index of vibration characteristic of actuator device

$$\gamma_{opp,i} = \frac{\int_0^{\mathrm{T}} \mathrm{H}(x_i \dot{x}_i) dt}{\int_0^{\mathrm{T}} 1 dt} \tag{31}$$

Equation (31) defines the proportional factor of how much velocity is in the same direction with displacement for the structural floor during the vibration.

5.3.3 Analysis of direction characteristic of STI control force

In the following, quantitative results of the indices defined above will be given to show the directional characteristic of active forces in the STI control scheme. From figure 47, the first index of each floor is found to be $\gamma_{1,i} \geq 90\%$ for $i = 1,2,\cdots,76$, which indicates that control force is being opposite to velocity at the possibility of more than 90%. Besides, the second index is $\gamma_{2,i} \cong 50\%$ for $i = 1,2,\cdots,76$, which means the active force is opposite to its velocity at the possibility of 50% during it vibrates against the equilibrium position. At last, the third index is found to be $\gamma_{opp,i} \cong 0.5$, which means the vibration of each actuator is almost balanced, nearly 50% against the equilibrium position and 50% towards the equilibrium position. Figure 48 shows the results of decomposing active control force into damping force and stiffness force, where the damping component is shown to be dominant, and this conclusion tally well with the results of another STI control scheme (Ou, 2003), where 20 actuators were employed and the resulting changes are 0.06% in the first modal frequency and 2.17% in the corresponding damping ratio.

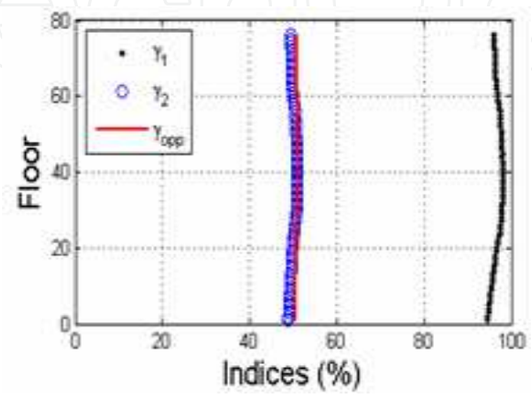

Fig. 47. Characteristic indices of active control force of STI control scheme

In the following, hysteresis loops of STI control force versus displacement and velocity are given in figure 49 and hysteresis loops of AMD control force are given in figure 50 for comparison. Here big difference can easily be seen between the two control schemes, where the STI control force is obviously some kind of damping force behavior.

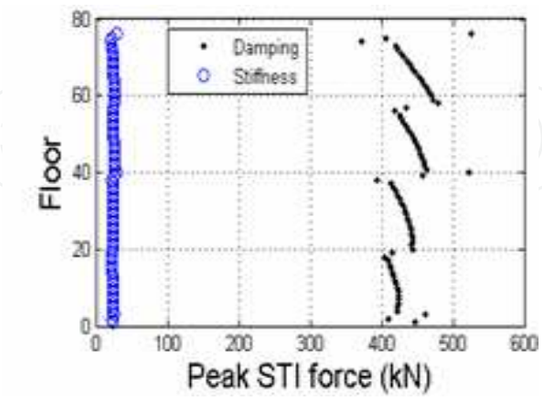

Fig. 48. Decomposing of active control force of STI control scheme

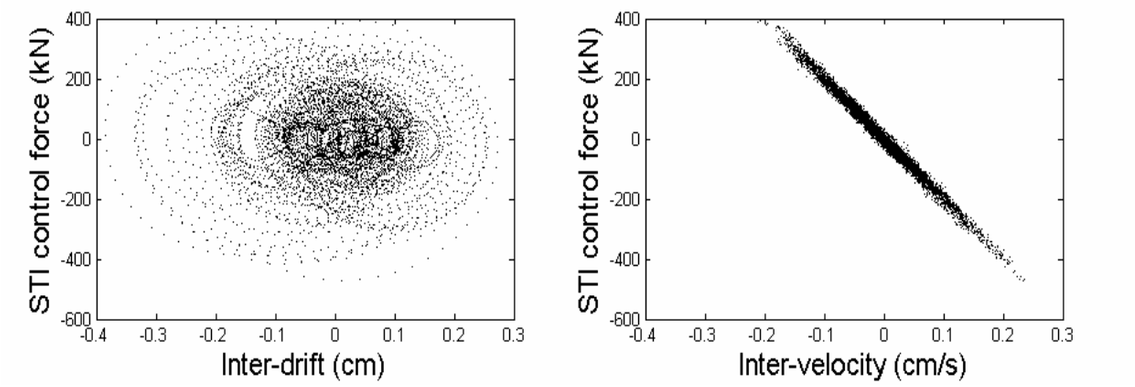

Fig. 49. Hysteresis loops of active control force of STI control scheme

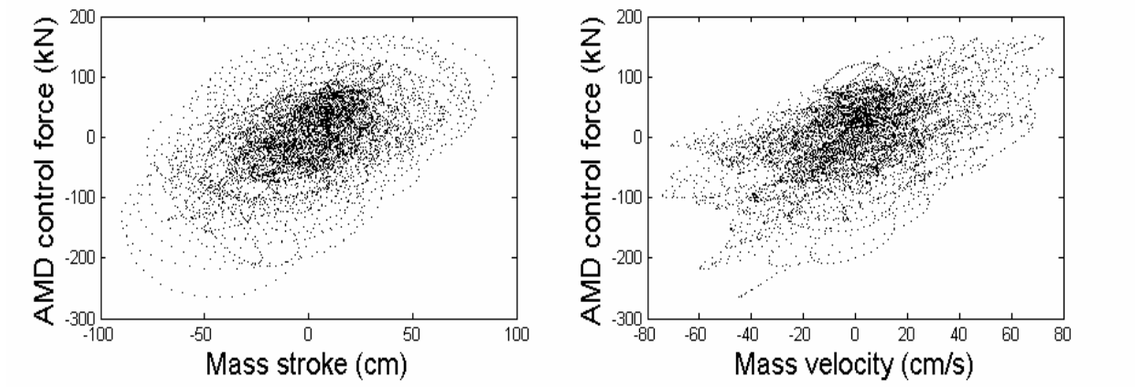

Fig. 50. Hysteresis loops of active control force of AMD control scheme

5.3.4 Energy characteristic of STI control force

In section 5.3.2, index γ_1 defines the direction characteristic of active control force, which stands for the ratio of area of virtual force defined in equation (26), which is the area of positive values divided by total areas. However, it is merely a measurement from the aspect of force magnitude, which does not take the effect of corresponding velocity into consideration. Noticing that there is such a relation exists between energy and force as $W = F \times v$, thus to improve equation (27), the proportional factor describing energy characteristic of control force can be defined as

$$\gamma_{Eopp} = \frac{\int_0^{\mathrm{T}} \mathrm{H}[-\dot{x}_i(t) \cdot u_i(t)] \cdot \left|\dot{x}_i(t) \cdot u_i(t)\right| dt}{\int_0^{\mathrm{T}} \left|\dot{x}_i(t) \cdot u_i(t)\right| dt} = \frac{E_{opposite}}{E_{total}} \tag{32}$$

Where $E_{opposite}$ stands for the energy of active control when the force is opposite to its velocity, and E_{total} stands for the total energy consumed by active control.

Figure 51 shows the energy indices distributed all through the entire structure of STI control scheme, where the maximum value of γ_{Eopp} is found to be 99.9977% and the minimum is 99.9492%, besides, the average value is 99.987%. Therefore, the result shows that nearly 100% control energy is distributed during the vibration course of force being opposite to velocity, which indicates that the force be damping control behavior.

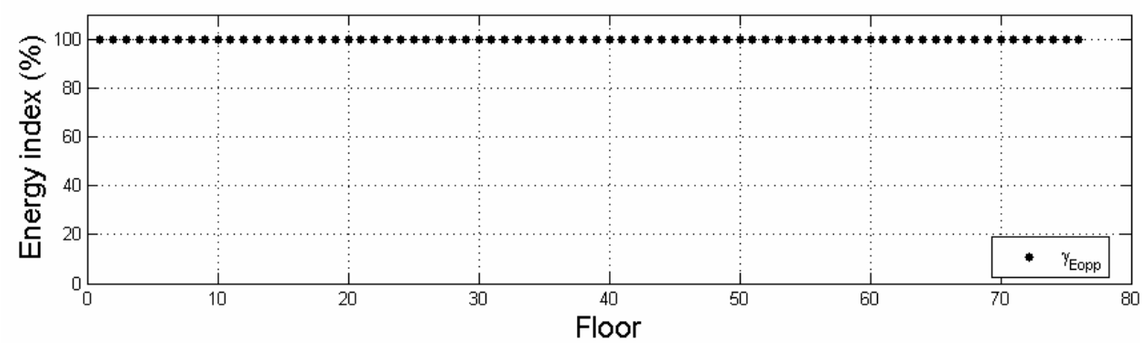

Fig. 51. Energy indexes of STI control force

So far, the active force of STI control scheme is proven to be intrinsicly damping force, thus, it is feasible to replace active actuators in this scheme by semi-active or even passive devices to achieve comparative pure active control performance. On the other hand, the force of AMD control doesn't possess the damping behavior, thus it can't be replaced by any semi-active device.

5.4 Structural adjacent wall active control

The reason of wasteful control cost of STI control scheme is owing to the existing of quits effect between control force and counter force for the adjacent structural floors. How to eliminate the disadvantageous is challenging. However, for the purpose of simulation, imagining a stiffen wall is placed beside the structure to be controlled, on which counter force of each actuator will be exerted, where the quits effect can be successfully excluded and we call such a scheme as structural adjacent wall (abbreviated as STA) active control.

Figure 52 shows the conception sketch of STA control. Although similar in name to adjacent-structures or coupled-structures control (Ying, 2004), they are absolutely different from the nature. In addition, STA control can be used to study the difference between AMD control and STI control from the aspect of function of actuators.

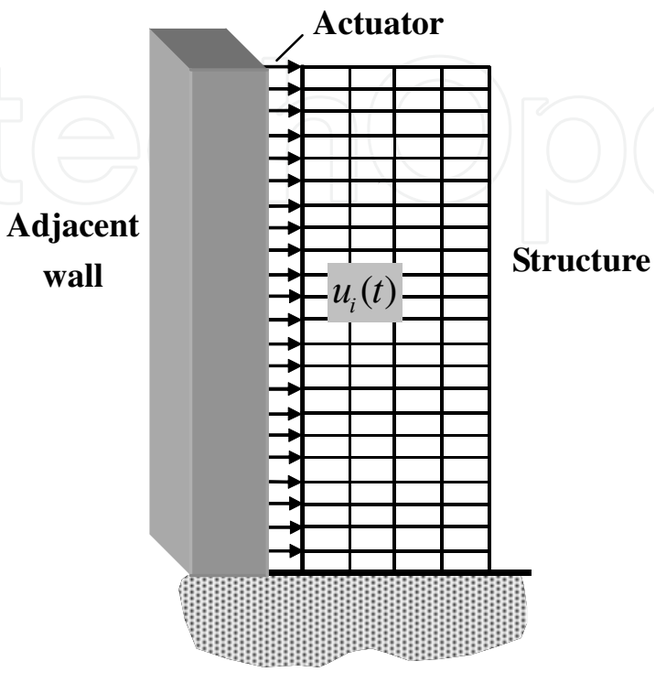

Fig. 52. Sketch of structural vibration control using STA control scheme

5.4.1 Comparison between STA control and AMD control

Similar approaches used in the above analysis of STI control will be introduced here to make a comparison between STA control and AMD control. Besides, for the purpose of analytical comparison, three control algorithms LQR, LQRY and LQG are all used again in order to exclude the possible differences caused by control algorithms and their parameters. In the following, table 6 gives the weight parameters of each control algorithm.

Control algorithms	LQR	LQRY、LQG
Q matrix	$[I]_{152\times152}$	$[I]_{228\times228}$
R matrix	$3\times10^{-10}\times[I]_{76\times76}\times\Phi_1$	

Table 6. Weight parameters of STA control scheme

According to the above settings, peak and RMS response of structural displacement and acceleration are shown in figure 53, where the control object is set to achieve comparative performance with AMD control.

Figure 54 shows the control force of each actuator corresponding to the above three control algorithms in STA scheme, where LQR control is shown to be the lowest in requirement of control force.

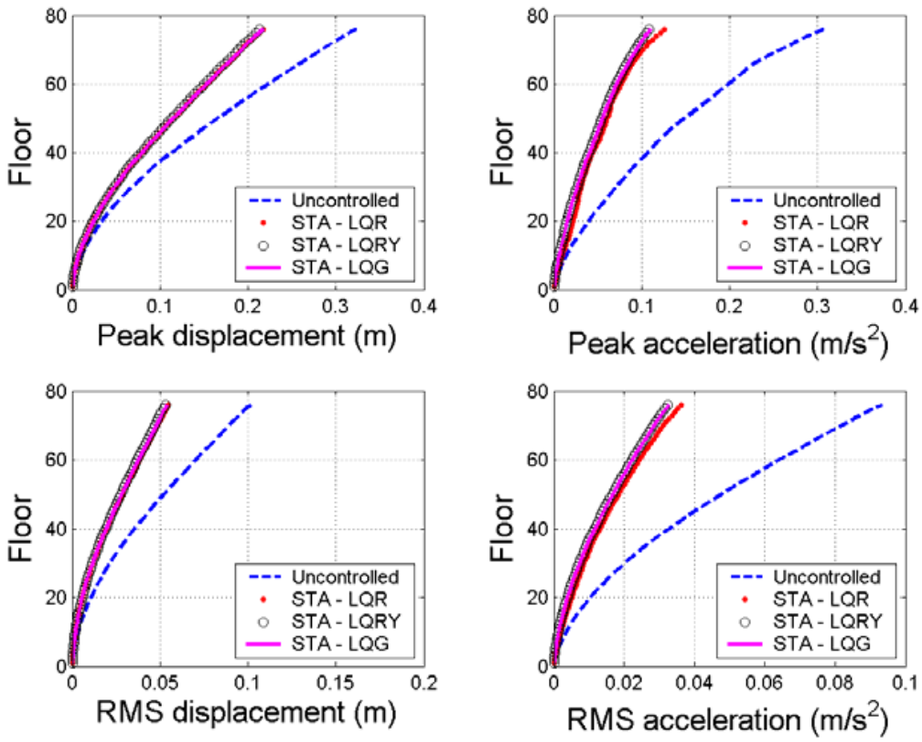

Fig. 53. Peak and RMS response of structure under STA control

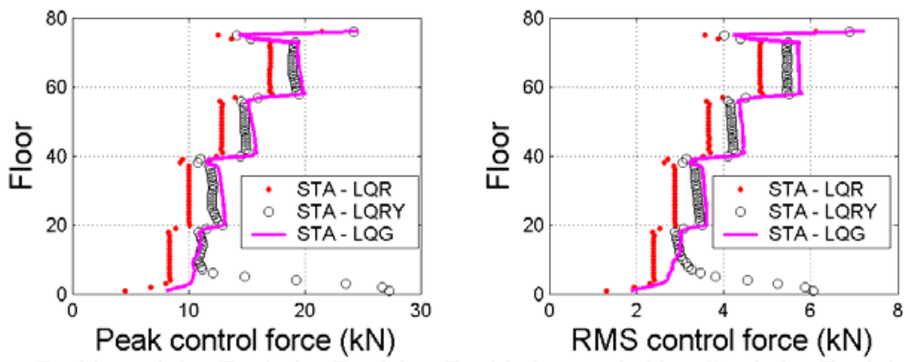

Fig. 54. Comparison of active force under three algorithms of STA control

Control scheme	Sum of control force(kN)		Reduction in displacement (%)		Reduction in acceleration (%)	
	Peak values	RMS values	Peak values	RMS values	Peak values	RMS values
AMD control	265	63.5	30.0	43.3	58.7	59.9
STI control	33288 (range: 527~372)	9500	33.2	46.5	61.3	62.7
STA control	905.7 (range: 4.6~21.5)	258.4	32.7	45.9	59.1	64.2

Table 7. Control forces and structural response results of three control schemes

So far, the results of structural response under three control schemes are studied respectively, and they were summarized in table 7. From the results, AMD control is shown to be the highest efficiency from the aspect of control effect over control effort, and STA control is inferior, whereas STI control is the lowest in control efficiency.

5.4.2 Analysis of characteristic of STA control force

Similar to indices defined in section 5.3.2, here the corresponding indices should be modified according to the changes of the coordinator system. Equation (27), (30) and (31) should be rewritten as

$$\gamma^{g}{}_{1,i} = \frac{\int_0^{\mathrm{T}} \mathrm{H}(-u_i\dot{y}_i)\,\mathrm{sgn}(-u_i\dot{y}_i)\left|u_i(t)\right|dt}{\int_0^{\mathrm{T}}\left|u_i(t)\right|dt} = \frac{\int_0^{\mathrm{T}} \mathrm{H}(-u_i\dot{y}_i)\left|u_i(t)\right|dt}{\int_0^{\mathrm{T}}\left|u_i(t)\right|dt} \tag{33}$$

$$\gamma^{g}{}_{2,i} = \frac{\int_0^{\mathrm{T}} \mathrm{H}(-u_i\dot{y}_i)\mathrm{H}(y_i\dot{y}_i)\,\mathrm{sgn}(-u_i\dot{y}_i)\left|u_i(t)\right|dt}{\int_0^{\mathrm{T}}\left|u_i(t)\right|dt} = \frac{\int_0^{\mathrm{T}} \mathrm{H}(-u_i\dot{y}_i)\mathrm{H}(y_i\dot{y}_i)\left|u_i(t)\right|dt}{\int_0^{\mathrm{T}}\left|u_i(t)\right|dt} \tag{34}$$

$$\gamma_{opp,i} = \frac{\int_0^{\mathrm{T}} \mathrm{H}(y_i\dot{y}_i)dt}{\int_0^{\mathrm{T}} 1dt} \tag{35}$$

Where y_i and $\dot{y}_i$ are displacement and velocity of the *ith* floor relative to the ground, and the other symbols take the meanings as defined before.

In addition, the energy index of equation (32) can be rewritten as

$$\gamma^{g}_{Eopp} = \frac{\int_0^{\mathrm{T}} \mathrm{H}[-\dot{y}_i(t)\cdot u_i(t)]\cdot\left|\dot{y}_i(t)\cdot u_i(t)\right|dt}{\int_0^{\mathrm{T}}\left|\dot{y}_i(t)\cdot u_i(t)\right|dt} \tag{36}$$

Figure 55 shows the indices corresponding to equation (33) ~ equation (36), where the control force is found to be almost opposite to velocity from the results of $\gamma_1{}^{g}$, especially from energy index $\gamma_{Eopp}{}^{g}$, and results of the other two indices are similar as before. Besides, figure 56 shows the results of decomposing active control force into damping force and stiffness force, where the damping component is shown to be dominant again.

Figure 57 shows the hysteresis loops between control force and displacement as well as velocity for STA control. From the results, the force is obviously shown to be some kind of damping force behavior.

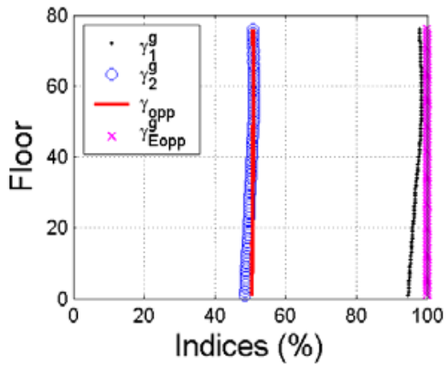

Fig. 55. characteristic indexes of control force of STA control scheme

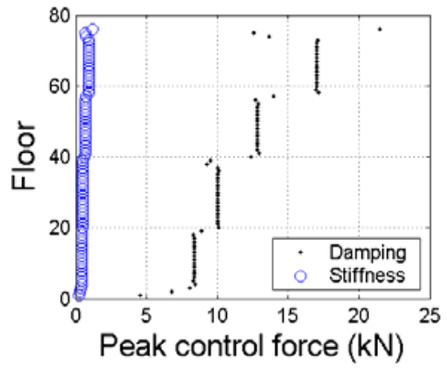

Fig. 56. decomposing of control force of STA control scheme

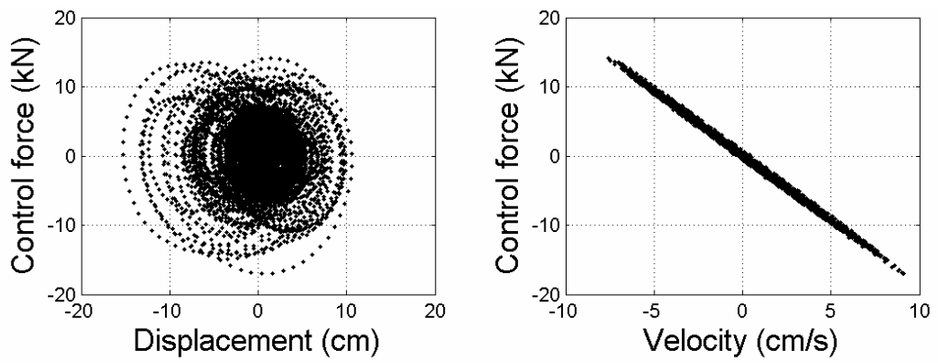

Fig. 57. Hysteresis loop of control force of STA control scheme

5.5 Discussions on similarity between AMD control and STA control

In the above two sections, three control schemes were compared from control effect to control cost, and the results show that AMD control is the best one compared with the other two schemes. Besides, STA control is shown to be rather better than STI control, and there must be some kind of relationship between AMD control and STA control. In the following, the numerical comparison between AMD control and STA control will be conducted to investigate their similarities as well as differences.

As shown in figure 53 and figure 54, three control algorithms of STA scheme are achieving almost at the same control results while at different cost, especially very large control forces are needed for the lower floors of structure in LQRY and LQG control case. This result indicate that forces at lower floors are ineffective for suppressing structural vibration, therefore, it would be better to place limited control devices onto higher floors as much as possible, and with the increase of height the control effectiveness will be enhanced. To the extreme situation, all actuators are concentrated onto the top floor, then the STA control is equal to AMD control, where both of the two control schemes use additional mass or wall other than the structure itself to provide supporting point for the counter force.

In the following, two special control cases, one is STA control with only one actuator at the top floor and the other is pure AMD control without damper and spring, are designed to

investigate the similarity between them. For the purpose of analytical comparison, the LQR control algorithm is being chosen, and the corresponding weight parameters are listed in the following table.

LQR algorithm	AMD control	STA control
Q matrix	$\begin{bmatrix} [I]_{76\times76} & & 0 \\ & [I]_{76\times76} & \\ 0 & & 0 \end{bmatrix}$	$[I]_{152\times152}$
R matrix	$r = 1\times10^{-11}$	

Table 8. Parameters of LQR control algorithm for AMD control and STA control

Figure 58 shows the comparison of AMD force versus STA force, where two forces are exactly the same, which indicates that under the above settings the two schemes have achieved at the same result as exerting control force onto the structure.

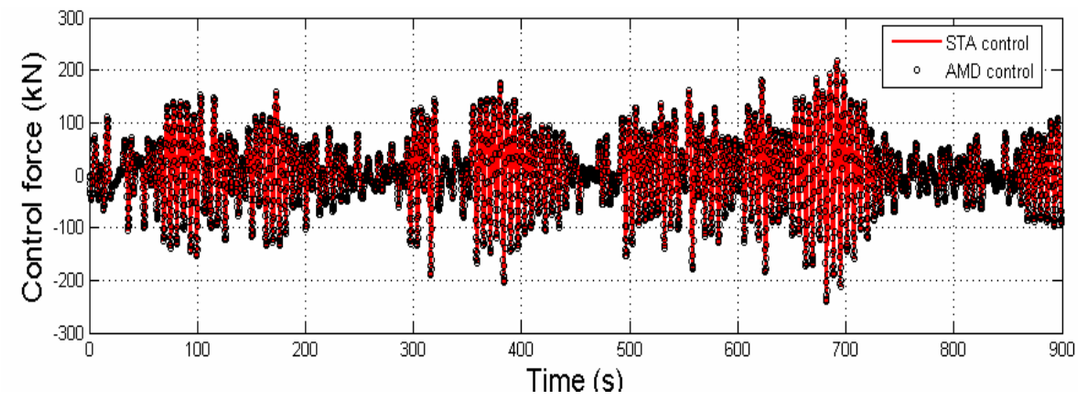

Fig. 58. Comparison of time history of control forces between AMD control and STA control

Except for the same control force, there are some other differences as well as similarity exist between the two control schemes. For AMD control, the force is generated by the actuator and the counter force is absorbed by mass, which oscillates on the top floor of the structure; Whereas for STA control, the stiffen wall is assumed to be infinity in stiffness, therefore stroke of the actuator is equal to the relative displacement of the top floor of the structure. Supposing that the mass of AMD increases to a certain amount until the mass stroke equals to that of STA actuator, then AMD control will be completely equivalent with STA control. This means we don't necessarily need a real "stiffen" wall, in fact a relative large mass will do, as well as no need for an adjacent wall, and a moving mass will do.

In order to validate the above assumption, the following analysis of mass ratio impact on characteristic of control force will be conducted. Here the variation range of mass ratio is chosen to be from 0.1% to 10%, which covers the range of interest.

As shown in figure 59, AMD-1 stands for the AMD control system with damper and spring element, and AMD-2 stands for the system without damper and spring, namely pure actuator based AMD control system. Besides, for comparison, the energy index of control force in STA scheme corresponding to equation (36) is also shown in figure 59 denoted with circle markers, and the exact value is 99.9993%.

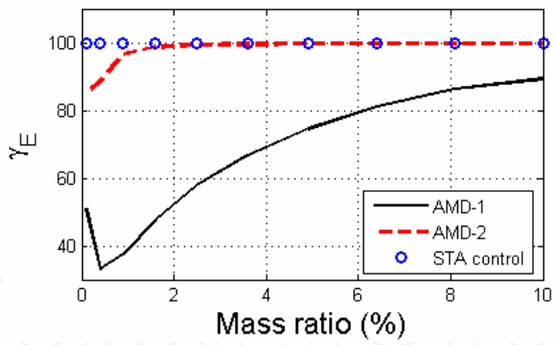

Fig. 59. Energy indexes of control force between AMD control and STA control

From the results, when mass ratio increases to 2% and thereafter, energy index of active force of AMD-2 system will be the same as STA control, which indicate that not only the envelope of force, as shown in figure 58, but also the intrinsic behavior is the same for AMD control and STA control. So far, AMD control is shown to be consistent with STA control under certain conditions, and we can come to the extension conclusions: 1) The effect of mass in the AMD system is equal to the wall in STA control scheme, which provides support point for the counter force; 2) AMD control is the simplest realization of STA control with smaller attached mass needed, and it is rather easier to be implemented than setting up an adjacent wall.

On the other hand, for AMD-1 system, the active force is affected by spring and damper element, thus the characteristic indices shown in figure 59 change differently with respect to mass ratio. Moreover, the effect of damper and spring on control performance is shown in figure 60

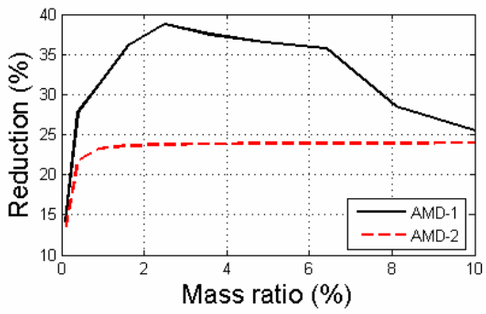

(a) Peak displacement of top floor

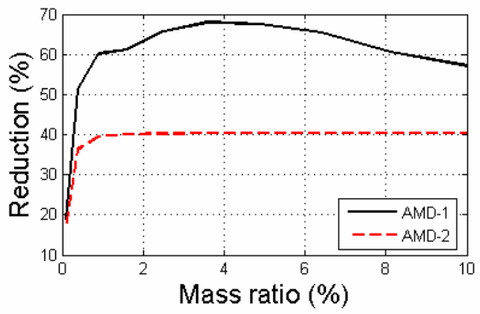

(b) Peak acceleration of top floor

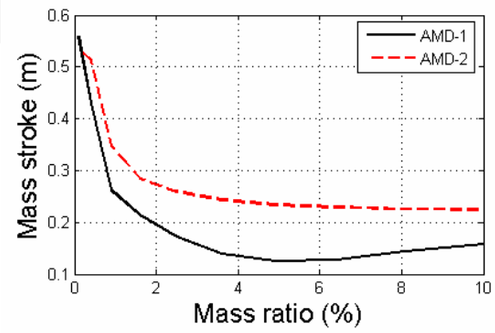

(c) Mass stroke of AMD system

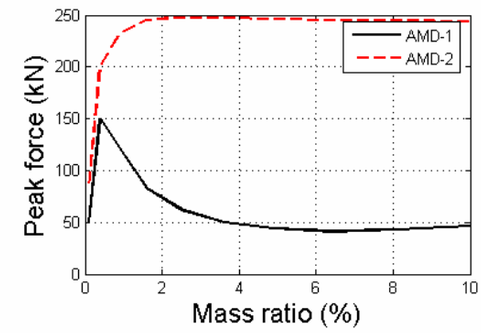

(d) Peak control force of AMD system

Fig. 60. Influence of mass ratio for AMD control scheme

From figure 60, the effect of mass in AMD-2 system is well demonstrated again, after the mass ratio increases to 2% as explained above, AMD control is equal to STA control, which will have no influence on control performance with increasing in mass weight. By comparison, owing to the interaction effect among actuator, damper and spring element, the ultimate control result of AMD-1 system is better than that of pure AMD system, besides the control cost, such as mass stroke and control force, is also reduced, which indicates that the complete construction of AMD control is better than STA control.

5.6 Summary on intrinsic mechanism of AMD control

In this section, three active control schemes, AMD control, STI control and STA control, have been studied under the background of wind-induced vibration control problem of the Benchmark 76-storey building structure, and main conclusions are achieved as follows:

1. Through comparison of control effect over control effort of the three control schemes, AMD control, with comparative control performance meanwhile at the minimum control cost, is shown to be most superior and economical. On the other hand, STA control is inferior and STI control is the worst one.
2. Indices denoting the direction and energy relationship between active force with velocity and displacement are developed to study the intrinsic behavior of control force in each control scheme. Through numerical analysis, quantitative results show that active force of STI control and STA control are damping force essentially, therefore it is feasible to replace active actuators in those schemes by semi-active or even passive control systems to achieve comparative performance of pure active control. However, the behavior of AMD control force is absolutely different, thus the actuator can't be replaced by any semi-active device.
3. Through similarity study between AMD control and STA control, the results well disclose the effect of mass piece in AMD system, which is similar to the wall in STA control scheme as providing supporting point for working of actuator, thus AMD control can be viewed as the simplest realization of STA control. Besides, the effect of mass as well as spring and damper in AMD control system is studied from a new aspect, and all the results show that AMD control is the most effective scheme for suppressing wind-induced vibration of the Benchmark building.

6. Application of AMD Control system

Based on the vibration analysis of the Guangzhou New TV Tower structure, the scheme of hybrid mass driver & variable damper (HMVD) is advanced to modify the common control systems. To choose the nodes at which the accelerations are measured to be used in Kalman estimator, the approach is proposed and adopted via the principle of modal superposition. Then the performance of the control system under T-year return periods is analyzed. And the control effectiveness is analyzed considering the variation of the damper-structure frequency tuning ratio.

6.1 Analytical model of the tower structure

The tower, as shown in figure 61, locates at the intersection of Guangzhou city new mid-axis and south bank of Zhujiang River, where is to be the central district of the city. The tower is designed for broadcasting, sightseeing, exhibiting purpose, etc. It will become the landmark

of Guangzhou City. Thus, it is obviously very important. The tower is 610m high, composed of a 454m high main tower and a 156m high antenna. The building is very slender, with the first natural period of 10.02 seconds. It is so slender and very sensitive to wind excitations. Therefore, studying the vibration control of the tower is remarkably significant.

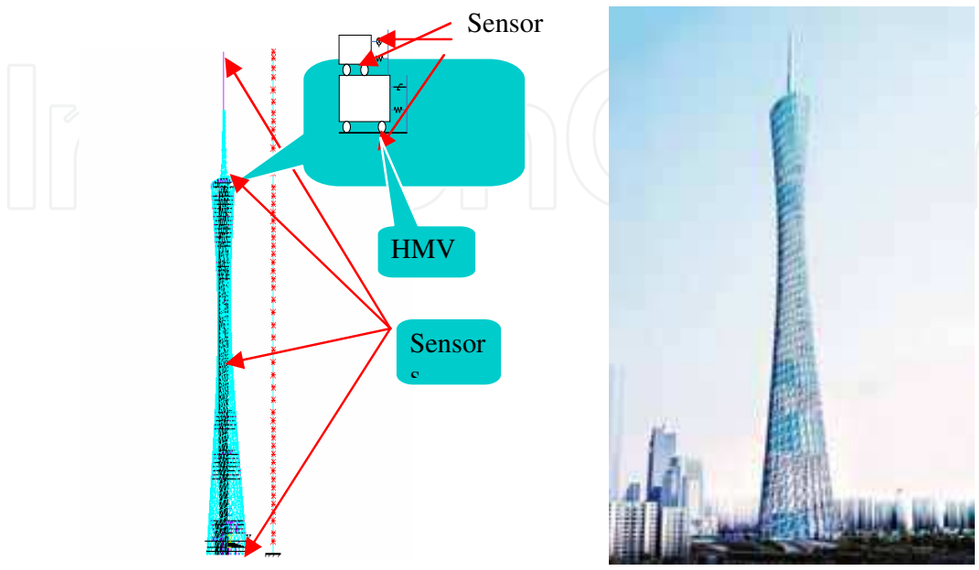

Fig. 61. Guangzhou New TV Tower structure

The wind reference pressure at the structure location is 0.55 KN/m² assuming a 100-year return period. The sort of the terrain roughness is C.

The main tower is a shear-flexural structure, composed of inner RC core tower and the steel frame outside, where the steel frame is composed of inclining columns of concrete filled steel tube, steel ring beams, and steel braces. To simplify the analytical model, the tower is discretized with a simple 106-degree-of-freedom lump mass model considering 53 concentrated mass nodes with two orthogonal lateral displacement DOF. The physical parameters, mass matrix M_s and stiffness matrix K_s, are obtained based on the FEM model using SAP2000. According to the Structural Preliminary Design Report, the damping ratios of its first two modes are 1.5%, respectively. And the Rayleigh damping matrix C_s is contributed. The dynamic properties of the 106 DOF model and the FEM model are compared and summarized in table 9.

Table 9 indicates that the 106 DOF model has almost the same dynamic characteristic with the FEM model. So it is appropriate for further analysis using the 106 DOF model.

Both time domain approaches and frequency domain approaches can be adopted to analyze the response and vibration control of the tower under wind excitation. The statistical characteristics of the response can be obtained through frequency domain approach. However, the necessary constraints, such as the peak value of the damper stroke and the control force, can not be explicitly considered in frequency domain method. Thus in this part, the linear elastic dynamic time-history analysis of the structure under random wind excitation is conducted.

Based on the Davenport spectrum, gust wind load time-histories are sampled. And three representative time histories are chosen for further analysis. Table 10 listed some responses at the top of the uncontrolled tower under these three wind samples.

Order of the modes	Natural period (s)			Descriptions of mode shapes	
	FEM model In SAP2000	106 DOF model	Relative error		
1	10.0135	9.9661	0.47 %	Global translational motion shape of 1st order	Along weak axis
2	6.9324	6.8978	0.51 %		Along strong axis
3	2.9074	2.8950	0.43%	Coupled mode Hape of main tower's 2nd order and antenna's 1st order	Along weak axis
4	2.4611	2.4626	0.06 %		Along strong axis

Table 9. Dynamic characters of the MDOF model and the FEM model

Analytical model	Load case	Displacement(m)		Acceleration(m/s2)	
		MAX	RMS	MAX	RMS
106 DOFmodel	Case1	0.890	0.3250	0.4182	0.1348
	Case2	0.900	0.3020	0.4316	0.1326
	Cas 3	0.876	0.3272	0.4024	0.1378

Table 10. Response at the top of the uncontrolled main tower under 100-year return period wind cases

6.2 Analysis and design of the control system

Previous studies have shown the advantages and the disadvantages of common control systems, such as viscous damper, tuned mass damper (TMD), active mass driver/damper (AMD), and hybrid mass damper (HMD). The conclusion is none of them could be used in this project directly. Further research proposed the scheme of hybrid mass driver & variable damper, which is abbreviated as HMVD. Figure 62 shows the main idea of the HMVD system to be introduced into this project. To avoid additional load and cost, the two 600-ton water tanks are taken as the mass in the passive part. It is proven effective and economical. Each tank is supported by three bilateral track supports along the two orthogonal axes. The steel-plate-laminated-rubber-bearing isolator is introduced to provide stiffness for the control system. Linear motor is introduced to drive the active subsystem, considering the requirement of the long stroke and the limitation of the installation space.

Computation results show that the stroke of the water tank along the strong axis of the tower can not exceed the limitation. So the control system is briefly designed as a TMD system along the strong axis.

6.2.1 Control analysis

The equation of motion of the 106 DOF model controlled with the HMVD is expressed by Eq. (37).

$$M_h\ddot{x} + C_h(t)\dot{x} + K_h x = F_w(t) + u_a(t) \tag{37}$$

Where, $x = \left[x_1, \cdots, x_n, y_1, \cdots, y_n, x_t, y_t, x_a\right]^T$; M_h, C_h and K_h are the mass matrix, damping matrix and the stiffness matrix of the tower-HMVD system respectively; $F_w(t)$ denotes the

wind load time-history; $u_a(t)$ denotes the driving force of the linear motor in the AMD subsystem.

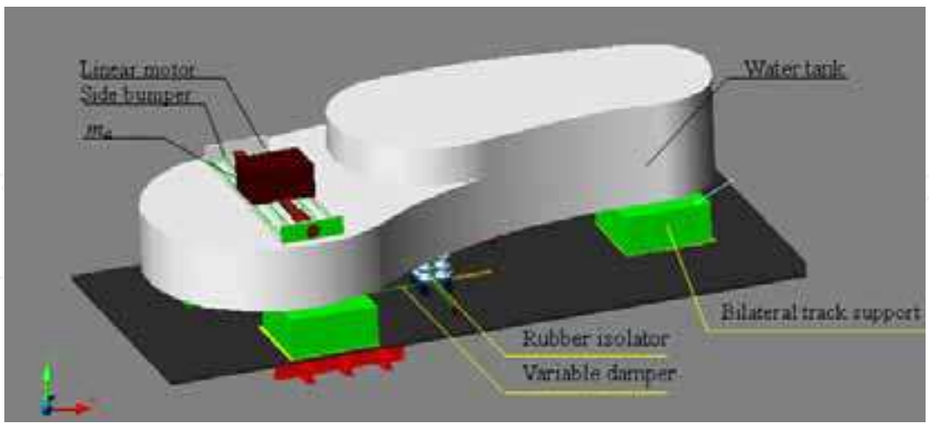

Fig. 62. Sketch of the HMVD system used in Guangzhou New TV Tower

The additional damping force provided by the additional damping Δc is considered as an external input force $F_{\Delta c}(t)$. Then the damping coefficient matrix C_h is invariable. And the equation of motion becomes:

$$M_h\ddot{x} + C_h\dot{x} + K_h x = F_w(t) + u_a(t) + F_{\Delta c}(t) \tag{38}$$

Where, $F_{\Delta c}(t) = \Delta c \times \Delta v(t)$, Δc is the additional damping coefficient, $\Delta v(t)$ denotes the relative velocity between the water tank and the floor on which the control system is installed.

The displacements, velocities, accelerations can be obtained via solving the Eq.(38).

6.2.2 Variable damper

There are two ways to design the damping coefficient for the traditional tuned mass damper control system. The first one is to set the damping ratio to the optimal case. With optimal damping, the control system can reduce the response of the tower under the regular wind load. But the stroke of the water tank will exceed the installation constraint under strong winds. Table 11 shows the stroke of the water tank with optimal damping under *T*-year return period wind loads.

Return period (year)		3	5	10	20	30	50	80	100	200
W_0 (KN/m²)		0.14	0.19	0.26	0.34	0.38	0.45	0.52	0.55	0.66
stroke (m)	Case 1	0.42	0.56	0.77	0.99	1.14	1.34	1.54	1.62	1.96
	Case 2	0.35	0.47	0.65	0.84	0.96	1.12	1.29	1.37	1.64
	Case 3	0.57	0.77	1.06	1.37	1.57	1.83	2.12	2.23	2.69

Table 11. Stroke of control system with optimal damping

The stroke of the water tank is limited to 1.2m by the installation space. However, as safety is considered, the stroke should not exceed 0.8m under 100-year return period wind excitations.

Another way to design the damping coefficient is to insure that the stroke of the water tanks will not exceed 0.8m under 100-year return period wind load. The damping coefficient designed in this way will be a big one, and will lead to much loss of effectiveness of the control system.

6.2.3 Role of the variable damper

After thorough analysis, a variable damper is introduced to reduce the stroke of the water tanks without much loss of the effectiveness under strong wind excitation. Considering the feasibility and reliability, the adopted variable damper scheme can be described as followings:

When the stroke is less than ±0.5m (phase A shown in figure 63), the damper is set to be the optimal damping coefficient c_{opt};

When the stroke is greater than ±0.5m, and the water tank is moving away from the equilibrium point (phase B shown in figure 63), the damper is set to be a much higher damping coefficient $c' = c_{opt} + \Delta c$, where Δc is the additional damping coefficient;

When the stroke is greater than ±0.5m, and the water tank is moving back to the equilibrium point (phase C shown in figure 63), the damper is set to be the optimal damping c_{opt} again.

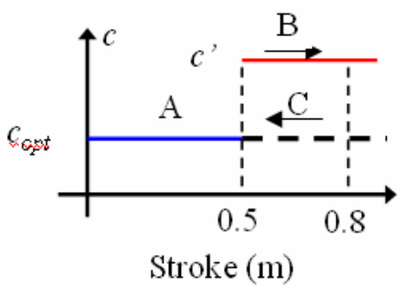

Fig. 63. Rule of the variable damper

6.2.4 Optimal damping coefficient

The optimal damping ratio of the control system is $\xi_{opt} = 0.08$. As the AMD system is fixed to the water tank except during few strong winds, the mass of the system should be considered as: $m_h = m_t + m_a = 1200 + 100 = 1300$ t. So the optimal damping coefficient is:

$$c_{opt} = 2m_h\omega_1\xi_{opt} = 2 \times 1300 \times 0.6305 \times 0.08$$
$$= 131.14KN \cdot s \cdot m^{-1}$$

6.2.5 Additional damping coefficient Δc

Figure 64 shows the relationship between the additional damping coefficient Δc and the maximum stroke of the water tank under 100-year return period wind load. The maximum stroke reduces as the additional damping coefficient Δc increases. To limit the stroke of the water tank to 0.8m under 100-year return period, the additional damping coefficient Δc should be no less than 1800 KN·s·m^{-1}. So the bigger damping coefficient in figure 63 taken as: $c' = c_{opt} + \Delta c = 131 + 1800 = 1931$ KN·s·m^{-1}. The following analysis is based on these parameters.

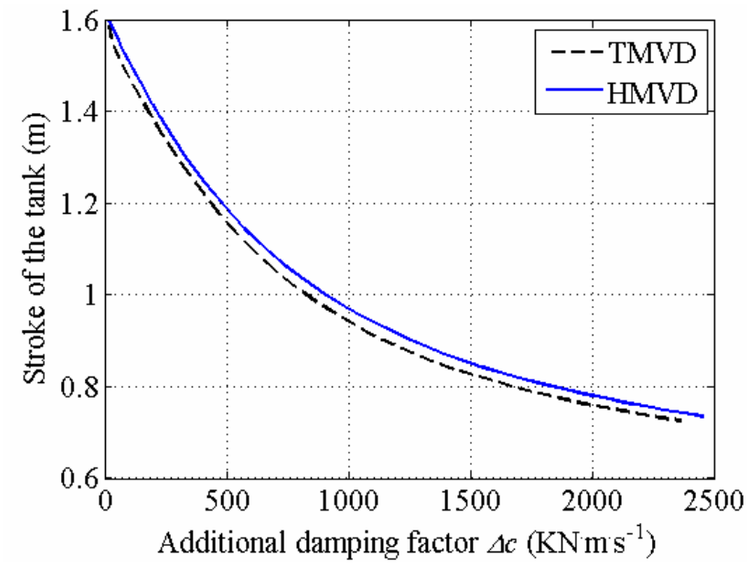

Fig. 64. Relationship between the maximum stroke and the additional damping ratio

6.3 Effectiveness of the control system

For uncontrolled case, TMVD control case and HMVD control case, the response at the top of the main tower is computed under *T*- year return periods wind loads. The control effectiveness of the displacement response and the acceleration response, besides the parameters of the TMVD system and the HMVD system are given in figure 65.

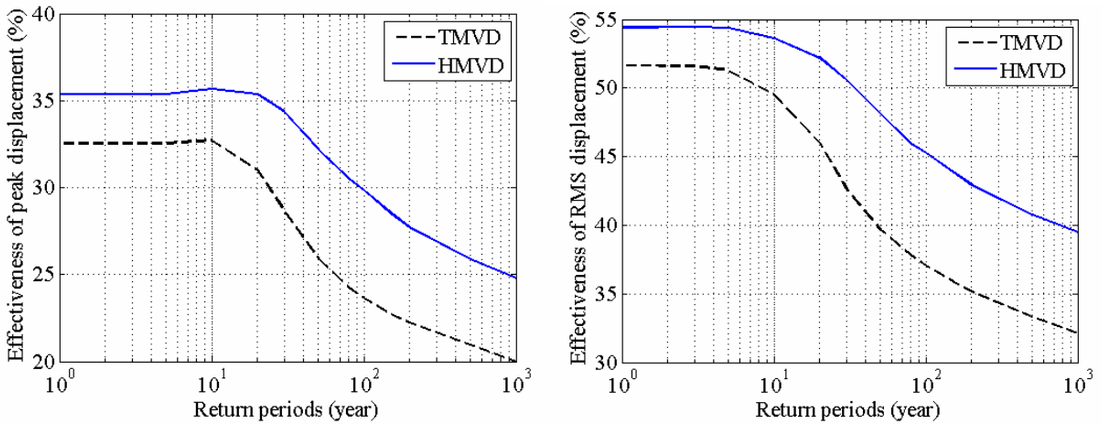

(a) Control effectiveness of peak displacement (b) Control effectiveness of RMS displacement

Fig. 65. Comparison on performance of passive and hybrid control system

Figure 65 shows that, the effectiveness is highest when the frequency tuning ratio is about 0.9 under 100-year return period. When the frequency tuning ratio varies, the effectiveness of the HMVD system varies on an even level, while the effectiveness of the TMVD system decrease drastically. That means the HMVD system is rather insensitive to the variation of the damper-structure frequency tuning ratio.

Based on the former comparison analysis of vibration control schemes for Guangzhou New TV Tower structure, the hybrid mass driver & variable damper (HMVD) control scheme is proposed and numerically studied in this section. Main conclusions can be achieved as: 1) The strategies to choose the measuring nodes for MDOF system is proposed based on the principle of modal superposition. According to this approach, the characteristic nodes of the main modes of the system are chosen, where the corresponding accelerations are measured to estimate the full states of the system. 2) The driving force of the AMD subsystem is calculated based on the LQG algorithm with Kalman estimator. 3) By introducing the variable damper, the optimal effectiveness of the control system is about 35%~50% with acceptable stroke under regular wind load. Under extreme strong winds (with bigger return period), the control system works in the active-passive hybrid mode. In this case, the stroke of the control system can be limited within the installation constraint range, keeping the remarkable effectiveness of 30%~45%. Thus the HMVD system is shown to be adaptive to the winds with different intensities. 4) The water tanks of the super-tall buildings are usually used as the mass of the tuning control system. While the mass of water may vary from time to time, leading to the variation of the optimal frequency tuning ratio of the damper and the decreased effectiveness of the control system. Further analysis indicates that the HMVD system is more robust to the damper-structure frequency tuning ratio. And this feature is especially beneficial for achieving better effectiveness of the HMVD control system.

7. Chapter summary

This chapter introduces some recent research works carried out in the Blast Resistance and Protective Engineering laboratory of Harbin Institute of Technology (HIT-BRPE) during the past few years. The EMD control system is shown to be effective and feasible for vibration control of civil engineering structures subjected to, such as earthquake, excitations. The DDVC based AMD control system is suitable for low frequency vibration and motion control. The innovative passive TRID system is applicable for rotation and swing motion control, whereas linear TMD system is shown to be invalid for structural swinging motion. All of the control systems mentioned in this chapter, whatever active or passive or hybrid, have a common characteristic, which is to utilize the mass inertia effect either to provide counter force support for functioning of actuator, *e.g.* AMD subsystem, or to provide gyrus or rotary inertia for anti swinging motion of suspended structure. Traditionally, these systems have been called Active Mass Damper/Driver (AMD) or Tuned Mass Damper (TMD), herein we want to emphasize the mass inertia effect and its functions. The basic is to be a necessary component of a control system, and more important is its way of working in the subsystem.

8. Acknowledgements

These researches are supported by the National Natural Science Foundation of China under grant No. 50608026 and 90815027, and the National Key Technology R&D Program under grant No. 2006BAJ03B06, and the National Major Fundamental Program under grant No. 2007CB714204. Associate Professor Li Jilong, Dr. Li Luyu, Dr. Liu Junlong, Mr. Xu Huaibing, Mr. Wu Zhiwu, Mr. Liu Chuan during their postgraduate studies in the Blast Resistance and Protective Engineering laboratory of Harbin Institute of Technology (HIT-BRPE Lab.), are acknowledged for their efforts in carrying out relevant experiments and analysis. Besides, the authors would like to give their sincere thanks to colleagues from Guangzhou

University and HIT-Shenzhen Graduate School for their effort and cooperation in application of control systems in the Guangzhou New TV tower project.

9. References

[1] Abdel-Rohman M. and Leipholz H.H.E. Structural Control by Pole Assignment Method. ASCE Journal of Engineering Mechanics, 1978, 104: 1157~1175.
[2] Battaini M., Yang G. and Spencer B. F. Jr. Bench-Scale Experiment for Structural Control. ASCE Journal of Engineering Mechanics. 2000, 126(2): 140~148.
[3] Brock J E. A Note on the Damped Vibration Absorbers. Journal of Applied Mechanics. 1946,13(4), A-284.
[4] Chu S.Y., Soong T.T., Reinhorn A.M. Real-time active control verification via a structural simulator. Engineering Structures, 2002, 24(3), 343~353.
[5] Den Hartog J.P. Mechanical Vibrations, 4th Ed, McG*raw-Hill,1956*.
[6] Dyke S. J., Spencer B. F., Belknap A. E., Ferrell K. J., Quast P., and Sain M. K. Absolute Acceleration Feedback Control Strategies for the Active Mass Driver. Proc. First World Conference on Structural Control, Pasadena, California. 1994, 2, TP1: 51~TP1: 60.
[7] Dyke S. J., Spencer B.F.Jr., Quast P., Kaspari D.C. Jr. and Sain M. K. Implementation of an Active Mass Driver Using Acceleration Feedback Control, Microcomputers in Civil Engineering: Special Issue on Active and Hybrid Structural Control. 1996, 11, 305~323.
[8] Haertling G. H. Rainbow Actuators and Sensors: A New Smart Technology. Proceedings of SPIE. 1997, 3040, 81~92.
[9] Haertling G. H. Rainbows–a New Type of Ultra–High Displacement Actuators. Am. Ceram. Soc. Bull. 1994, 73~96.
[10] Housner G. W., Bergman L. A., Caughey T. K., Chassiakos A. G., Claus R. O., Masri S. F., Skelton R. E., Soong T. T., Spencer B. F. and Yao J. T. P.. Structural Control: Past, Present, and Future. J Engng Mech, ASCE. 1997, 123(9): 897~971.
[11] Kuo B. C. Automatic Control Systems. 7th Edition, Prentice-Hall, 1995.
[12] Lee D. J. Use of Accelerometer in Precision Motion Control Systems Design and Its Applications to Linear Motors. Ph.D Dissertation of California at Berkeley. (Supervised by Prof. M. Tomizuka),2002.
[13] Liu Junlong, Zhang Chunwei, Ou Jinping. Modeling and numerical analysis on direct driving active mass driver control system for structural vibrations, Journal of Vibration Engineering, v 21, n 4, p 323-328, August 2008 Language: Chinese.
[14] Mita A., Kaneko M. Hybrid versus tuned or active mass dampers for response control of tall buildings. The 1st international conference on motion and vibration control, Yokohama, Japan, 304-309, 1992.
[15] Nerves A.C., Krishnan R. A strategy for active control of tall civil structures using regenerative electric actuators. Proc., 11th ASCE Eng. Mech. Spec. Conf., Ft. Lauderdale, FL, 1996, 503-506.
[16] Ou J. P. Structural vibration control – active, semi-active and smart control, science press, 2003
[17] Ou Jinping, Zhang Chunwei. Modeling and dynamical testing of an innovative electro-magnetic active mass driver control system for structural vibration, Chinese High Technology Letters, v 17, n 4, p 382-388, April 2007 Language: Chinese.
[18] PMAC motion servo controller, user's manual (CD-ROM), 2003.
[19] Quanser Consulting Inc. Active Mass Damper – Two-Floor (AMD-2), User Manual, 2002.

[20] Quast P., Sain M.K., Spencer B.F. Jr. and Dyke S.J. Microcomputer Implementations of Digital Control Strategies for Structural Response Reduction. Microcomputers in Civil Engineering: Special Issue on New Directions in Computer Aided Structural System Analysis, Design and Optimization, 1995, Vol. 10, pp. 1325.
[21] Rana R., Soong T.T. Parametric Study and Simplified Design of Tuned Mass Dampers. Engineering Structures, 1998, 20(3), 193-204.
[22] Ricciardelli F., Pizzimenti A. D., Mattei M. Passive and active mass damper control of the response of tall buildings to wind gustiness. Engineering structures, 2003, 25, 1199-1209.
[23] Schmitendorf W E, Faryar J and Yang J N. Robust Control Techniques for Building under Earthquake Excitation[J]. Earthquake Engineering and Structural Dynamics, 1994,23: 539–552.
[24] Scruggs J. T. and Iwan W. D. Control of a Civil Structure Using an Electric Machine with Semiactive Capability. ASCE Journal of Structural Engineering. 2003, 129(7): 951~959.
[25] Soong T. T.. Active Structure Control Theory and Practice. Longman Scientific & Technical. New York, USA. 1990.
[26] Spencer B. F. Jr, Dyke S J and Deoskar H S. Benchmark Problems in Structural Control: Part I – Active Mass Driver System. Earthquake Engineering and Structural Dynamics. 1998, 27(11), 1127~1139.
[27] Spencer B. F. Jr. and Sain M. K., Controlling Buildings: A New Frontier in Feedback, IEEE Control Systems Magazine: Special Issue on Emerging Technologies (Tariq Samad Guest Ed.). 1997, 17(6): 19~35.
[28] Spencer B. F.Jr. and Nagarajaiah S. State of the Art of Structural Control. ASCE Journal of Structural Engineering. 2003, 129(7): 845~856.
[29] Warburton G.B. Optimal Absorber Parameters for Various Combination of Response and Excitation parameters. Earthquake Engineering and Structural Dynamics, 1982, 10, 381-401.
[30] Warburton G.B., Ayorinde E.O. Optimum Absorber Parameters for Simple Systems.Earthquake Engineering and Structural Dynamics. 1980, 8, 197-217.
[31] Wu Zhiwu.(2008). Modeling and control scheme analysis on spatial planar-rotational-coupling motions of suspensory structures. Master thesis of Harbin Institute of Technology,2008. Language: Chinese.
[32] Xue D. Y. Design and analysis of feedback control system – the application of MATLAB. Tsinghua University press, 2000.
[33] Yang G. Large-Scale Magnetorheological Fluid Damper for Vibration Mitigation: Modeling, Testing and Control, Ph.D dissertation, University of Notre Dame. 2001.
[34] Yang G., Spencer B. F.Jr., Carlson J. D. and Sain M. K. Large-Scale MR Fluid Dampers: Modeling and Dynamic Performance Considerations, Engineering Structures. 2002, 24(3): 309~323.
[35] Yao J. T. P. Concept of Structure Control. Journal of Structure Division, ASCE 1972, 98(ST7): 1567~1574.
[36] Yie Y.Y. Principles and applications of linear motors. Mechanical industrial press, Beijing, 2000.
[37] Yoshida I., Kurose H., Fukui S., Iemura H. Parameter identification on active control of a structural model. Smart Materials and Structures, 1995, 4(1A), A82~A90.
[38] Zhang Chunwei, Li Luyu, Ou Jinping. Swinging motion control of suspended structures: Principles and applications, International Journal of Structural Control and Health Monitoring, 2009 (published online 10.1002/stc.331.

[39] Zhang Chunwei, Ou Jinping. Analysis of active mass driver control against wind-wave coupled excitations for deep-water fixed jacket platform structures, Journal of Harbin Institute of Technology, v 37, n SUPPL. 1, p 198-201, May 2005 Language: Chinese.
[40] Zhang Chunwei, Ou Jinping. Characteristic indices and analysis of active control forces in active mass driver control system for structural vibration, Engineering Mechanics, v 24, n 5, p 1-9, May 2007 Language: Chinese.
[41] Zhang Chunwei, Ou Jinping. Characteristic of Control Force in Structure- Active Mass Driver Control System, Journal of Vibration Engineering, 2010, 23(1), 1-6. Language: Chinese
[42] Zhang Chunwei, Ou Jinping. Characteristics of Active Forces in Structural Hybrid Mass Damper Control Systems, 2004 ANCER Annual Meeting Networking of Young Earthquake Engineering Researchers and Professionals, July 28-30, 2004, Honolulu, Hawaii, USA.
[43] Zhang Chunwei, Ou Jinping. Closed-loop control strategies and dynamical tests of the electromagnetic mass damper control system, Journal of Vibration Engineering, v 20, n 3, p 213-218, June 2007 Language: Chinese.
[44] Zhang Chunwei, Ou Jinping. Control strategies and experimental verifications of the electromagnetic mass damper system for structural vibration control, Earthquake Engineering and Engineering Vibration, 2008, 7(2), 181-192.
[45] Zhang Chunwei, Ou Jinping. Control Strategies and Experiments of the Electromagnetic Mass Damper Control System for Structural Vibration, Journal of Sound and Vibration Control, 2006, 26(5), 9-13. (in Chinese)
[46] Zhang Chunwei, Ou Jinping. Control Structure Interaction of Electromagnetic Mass Damper System for Structural Vibration Control, ASCE Journal of Engineering Mechanics, 2008, 134(5), 428-437
[47] Zhang Chunwei, Ou Jinping. Evaluation Indices and Numerical Analysis on Characteristic of Active Control Force in Structural Active Mass Driver Control System, Pacific Science Review, 2007, 9(1), 115-122.
[48] Zhang Chunwei, Ou Jinping. Intrinsic Behavior Analysis of Active Force in HMD Systems, the Eighth International Symposium on Network and Center-Based Research for Smart Structures Technologies and Earthquake Engineering, July 6-9, 2004, Osaka, Japan.
[49] Zhang Chunwei, Ou Jinping. Modeling and testing for electromagnetic mass damper and structure coupled system, Journal of Vibration Engineering, v 19, n 3, p 289-295, September 2006 Language: Chinese.
[50] Zhang Chunwei, Ou Jinping. Shaking table tests of electromagnetic mass damper system for control of structural seismic response, Journal of Earthquake Engineering and Engineering Vibration, 2006, 26(2), 104-110. (in Chinese)
[51] Zhang Chunwei, Xu Huaibing, Li Luyu, Ou Jinping. Parametric impact analysis and experimental verifications of TRID system for structural pendular vibration control, I Parametric impact analysis and Bench-scale experimental verifications, Journal of Control Theory and Application, CCTA090432, 2010 in press. Language: Chinese
[52] Zhang Chunwei. Electromagnetic AMD systems and their relevant theory and experiments for structural vibration control. Ph.D thesis of Harbin Institute of Technology, 2005.
[53] Zhang Chunwei. Some problems on blast resisting, anti-shocking and vibration control of structures. Postdoctoral Research Report of Harbin Institute of Technology, 2007
[54] Zhang Y.F., Iwan W.D. Active interaction control of civil structures. Part 2: MDOF systems. Earthquake Engineering and Structural Dynamics, 2002, 31(1), 179~194.

Vibration Control

Edited by MickaÃƒÂ«l Lallart

ISBN 978-953-307-117-6
Hard cover, 380 pages
Publisher Sciyo
Published online 18, August, 2010
Published in print edition August, 2010

Vibrations are a part of our environment and daily life. Many of them are useful and are needed for many purposes, one of the best example being the hearing system. Nevertheless, vibrations are often undesirable and have to be suppressed or reduced, as they may be harmful to structures by generating damages or compromise the comfort of users through noise generation of mechanical wave transmission to the body. the purpose of this book is to present basic and advanced methods for efficiently controlling the vibrations and limiting their effects. Open-access publishing is an extraordinary opportunity for a wide dissemination of high quality research. This book is not an exception to this, and I am proud to introduce the works performed by experts from all over the world.

InTech Europe
University Campus STeP Ri
Slavka Krautzeka 83/A
51000 Rijeka, Croatia
Phone: +385 (51) 770 447
Fax: +385 (51) 686 166
www.intechopen.com

InTech China
Unit 405, Office Block, Hotel Equatorial Shanghai
No.65, Yan An Road (West), Shanghai, 200040, China
中国上海市延安西路65号上海国际贵都大饭店办公楼405单元
Phone: +86-21-62489820
Fax: +86-21-62489821

IntechOpen